A Membrane-Disruptive Action of VBIT-4 Challenges Its Role as a Widely Used VDAC Oligomerization Inhibitor

Varun Ravishankar[1*], Luís Borges-Araújo[2,3*], Elodie Lafargue[4], Deborah Byrne[5], Nicolas Buzhinsky[4], Mya S. Wolfe[6], Nina A. Bautista[6], Bethel G. Beyene[6], Motahareh G. Larimi[6], Jean-Pierre Duneau[1], James Sturgis[1], Megha Rajendran[6], Sergey M. Bezrukov[6], Ignacio Casuso[4], Tatiana Rostovtseva[6], Lucie Bergdoll[1#]

1. Laboratoire d'Ingénierie des Systèmes Macromoléculaires, CNRS, UMR 7255 - Aix Marseille Université, 31 Chemin Joseph Aiguier, 13402 Marseille, France

2. Laboratoire de Biologie et Modélisation de la Cellule, CNRS, UMR 5239, Inserm, U1293, Université Claude Bernard Lyon 1, Ecole Normale Supérieure de Lyon, Lyon, France

3. Centre Blaise Pascal de Simulation et de Modélisation Numérique, Ecole Normale Supérieure de Lyon, Lyon, France

4. U1325 Aix-Marseille Université, INSERM, DyNaMo, Turing Centre for Living System, Marseille, France

5. Protein Expression Facility, Aix Marseille Université, CNRS, IMM, 13402, Marseille, France

6. *Eunice Kennedy Shriver* National Institute of Child Health and Human Development, NIH, Bethesda, Maryland, 20892, USA

* : equal contribution
\# : to whom correspondence should be addressed, lbergdoll@imm.cnrs.fr

Keywords: VBIT-4, VDAC, membrane destabilization, lipid pores, toxicity

Abstract:

VDAC, the most abundant protein in the outer mitochondrial membrane, plays a central role in mitochondrial physiology. Its oligomerization has been contemplated to be involved in critical processes such as mtDNA release and apoptosis, yet the underlying molecular mechanisms remain poorly defined. VBIT-4, a small molecule widely used as a VDAC1 oligomerization inhibitor, has seen extensive applications over the past five years without proper mechanistic characterization. Using high-speed atomic force microscopy, we directly visualized VDAC1 oligomerization in planar lipid membranes and examined the effects of VBIT-4. Unexpectedly, VBIT-4 partitioned into lipid bilayers at micromolar concentrations and disrupted membrane structure even in the absence of VDAC1. Complementary approaches—including single-channel electrophysiology, microscale thermophoresis, and coarse-grained molecular dynamics—confirmed the membrane partitioning and destabilizing effects of VBIT-4. The compound also induced VDAC1-independent cytotoxicity in HeLa cells at concentrations above 10 μM. Our findings demonstrate that VBIT-4 disrupts membrane integrity by partitioning into lipids and inducing membrane defects rather than specifically inhibiting VDAC1 oligomerization, highlighting the need for caution when interpreting results and the importance of revisiting conclusions drawn from its prior use.

Introduction:

The Voltage-Dependent Anion Channel (VDAC) is a pivotal protein in the mitochondrial outer membrane (MOM), constituting more than 50% of its total protein content[1,2]. As the primary gateway between the mitochondria and the cytosol, VDAC facilitates the transport of ions and metabolites, such as ATP and ADP, playing a central role in cellular energy metabolism. Beyond its transport function, VDAC regulates diverse mitochondrial functions, including apoptosis[3–6], calcium homeostasis[7–10]mitochondrial DNA release[11], and lipid scrambling[12]. VDAC also acts as a mitochondrial anchor, recruiting and coordinating interactions with many cytosolic proteins[13–15]. In mammals, there are three VDAC isoforms—VDAC1, VDAC2, and VDAC3, each capable of transporting ions and metabolites[16,17] yet contributing uniquely to mitochondrial function through distinct protein interactions and pathway involvement.

VDAC is often highlighted as a promising drug target due to its involvement in numerous pathological pathways[18–20]. However, its central role in mitochondrial physiology and the absence of a "well-defined catalytic cleft"[20] make it a challenging target, as modulating its activity could affect several cellular pathways. Additionally, the incomplete understanding of VDAC's multifaceted functions—from metabolite exchange to apoptosis regulation—remains a major obstacle to designing effective therapeutics. Among these functions, the propensity of VDAC to form higher-order assemblies has emerged as a particularly intriguing aspect, raising interest in its oligomerization as a more selective therapeutic entry point.

VDAC oligomerization is now recognized to underlie essential physiological functions, including mitochondrial DNA release[11], lipid scrambling[12], mitochondrial organization[21], and interaction with MOM proteins[22] — processes central to mitochondrial dynamics and stress adaptation. In recent years, VDAC oligomerization has attracted increasing interest as a therapeutic target. However, these so-called "oligomers" are in fact heterogeneous lipid–protein clusters rather than well-defined assemblies[1,2,23], making them challenging to target specifically.

In 2016, Ben-Hail *et al.* developed VBIT-4—a small molecule inhibitor of VDAC1 oligomerization—using a combination of cross-linking and cell survival assays[24]. Since its development, VBIT-4 has been employed to probe the role of VDAC1 oligomerization in various diseases, including lupus erythematosus[11], atrial fibrosis[25], amyotrophic lateral sclerosis (ALS)[26], inflammatory bowel disease[27], Alzheimer's disease (AD)[28], diabetic vasculopathies[29], ß-cell dysfunction[30], diabetic retinopathy[31], chronic pain[32], and epilepsy[33]. However, despite its broad use, the precise mechanism by which VBIT-4 modulates VDAC1 and its oligomerization remains unresolved.

High-speed atomic force microscopy (HS-AFM) recently enabled nanometer-scale visualization of VDAC1 oligomerization in real time under near-physiological conditions[23], revealing that lipids are key regulators of VDAC1 assembly and that disruption of physiological lipid composition destabilizes native-like VDAC1 clusters. Here, using a planar lipid bilayer system and the unique capabilities of HS-AFM, we directly examined the effects of VBIT-4 on VDAC1 oligomerization. Unexpectedly, micromolar concentrations of VBIT-4 caused pronounced membrane permeabilization and bilayer defects—even in the absence of VDAC1. Complementary analyses—including single-channel electrophysiology, microscale thermophoresis, and molecular dynamics simulations—confirmed that VBIT-4 partitions into the lipid bilayer and perturbs its physical properties, independently of VDAC.

Results:

VBIT-4-Induces Perturbations in VDAC1-Containing Membranes

HS-AFM allows label-free, real-time imaging of nanoscale dynamics under near-physiological conditions, making it ideal for assessing small molecule effects on membrane integrity and VDAC oligomerization. We used it to examine the impact of VBIT-4 on well-characterized VDAC1 clusters in POPC:POPE:cholesterol (PC/PE/chol 60:32.5:7.5, w:w ratio) membranes, reconstituted with or without VDAC1, and adsorbed onto a mica substrate[23].

Before VBIT-4 addition, membranes containing VDAC1 exhibit a well-defined topography (Figure 1A): they display extended honeycomb assemblies interspersed with lipid-rich zones, where the protein establishes an optimal lipid-protein ratio[23]. At 1 µM VBIT-4, the first signs of structural disruption appear as small perforations a few nanometers wide and deep (Figure 1B*), indicating localized lipid bilayer destabilization without structural alteration of VDAC1 clusters. Analysis of the height profile (bottom) allows us to differentiate between the height of VDAC1 and the defects induced by VBIT-4 (*), which are located deeper, indicating possible local insertion or disorganisation of the membrane. At 10 µM VBIT-4, the effect intensifies, with an increased number and size of perforations (Figure 1C*). High-resolution AFM images show a clear morphological distinction between the pores of VDAC1, which retain a well-organised honeycomb structure (Box 1), and the irregular defects caused by VBIT-4. VBIT-4-induced perforations are deeper, primarily in the lipid domains adjacent to VDAC1. The high-resolution AFM images show a clear morphological distinction between the pores of VDAC1, which retain a well-organised honeycomb structure (Box 1), and the irregular defects caused by VBIT-4 (confirmed by section 2. The height profiles (i and ii) confirm that the VBIT-4 pores are wider and deeper than those formed by VDAC1. The absence of major structural changes in VDAC1 clusters suggests that VBIT-4 preferentially targets the lipid matrix rather than modifying VDAC1 assemblies.

VBIT-4-Induced Membrane Perturbation in Protein-Free Lipid Bilayers

To examine the impact of VBIT-4 on lipid bilayers properties by HS-AFM, we next tested protein-free membranes. Control membranes exhibited a homogeneous topography without apparent defects (Figure 1D). Addition of 1 µM VBIT-4 already modifies the membrane structure by inducing isolated protrusions up to tens of nanometers in diameter (height profile in box, Figure 1E). This observation suggests the formation of higher-order oligomers or aggregates of VBIT-4 (Supplementary Figure 1), rather than individual molecules (VBIT-4 is ~2×0.5 nm when neutral and ~1.2×0.5 nm when charged). At 5 µM, these features became more prominent, producing extensive membrane deformations, including transmembrane defects (Figure 1F). At 50 µM—the concentration used in cellular assays—the disruptions intensified, and at 100 µM, HS-AFM revealed nanometer-scale perforations consistent with membrane rupture (Figure 1G,H). Height profile analysis confirmed that VBIT-4 induces defects sufficient to compromise bilayer integrity. Thus, in the absence of VDAC1, VBIT-4 alone is capable of progressively destabilizing the membrane, ultimately leading to structural failure at high concentrations.

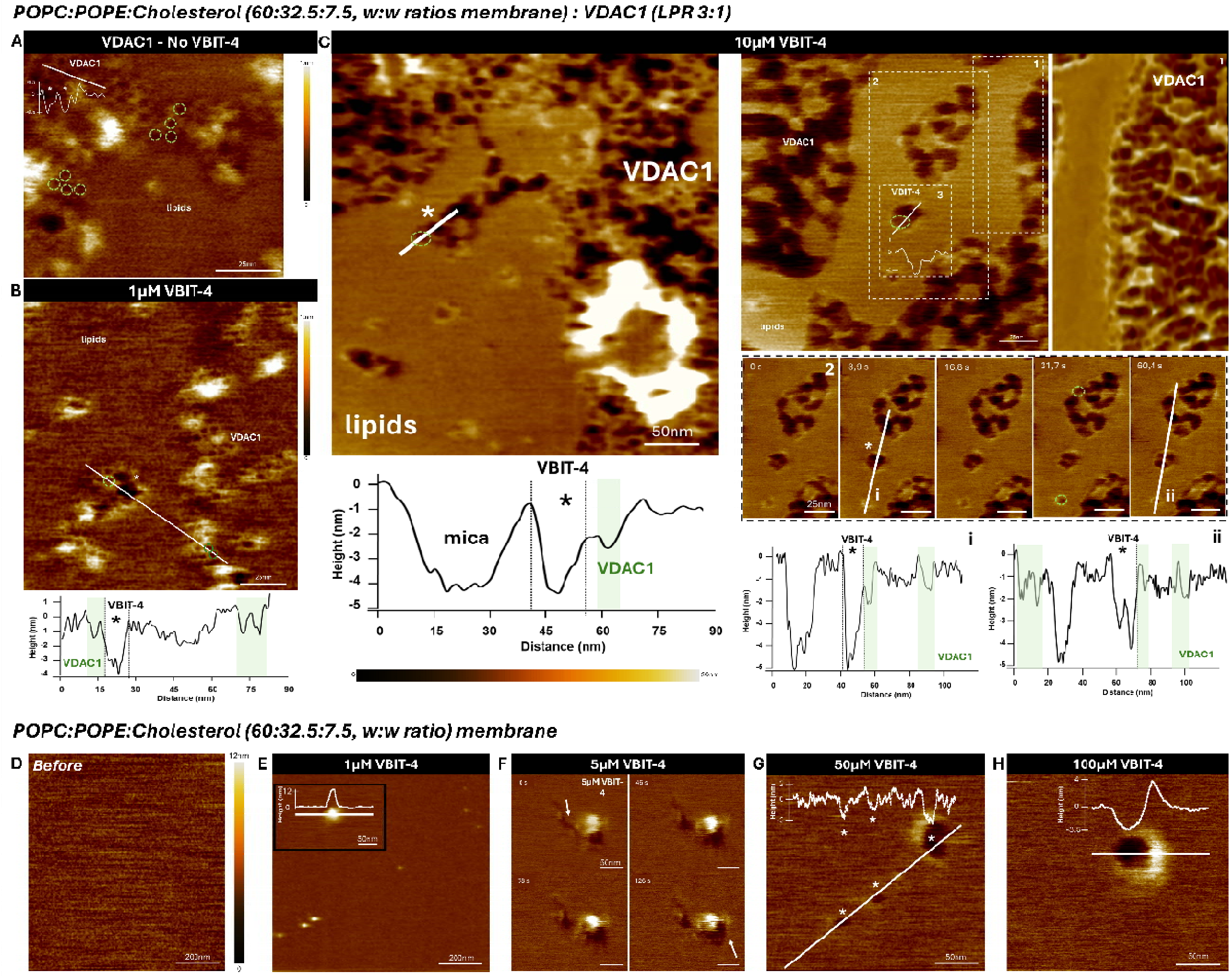

Figure 1. VBIT-4 induces defects in POPC:POPE:Chol (60:32.5:7.5) bilayers, independently of VDAC1 presence. VDAC1 reconstituted into liposomes was adsorbed onto a mica surface for AFM imaging. **Upper panels:** AFM image and associated height profile before (**A**) and after addition of 1μM (**B**) and 10μM (**C**) VBIT-4 molecule to lipid bilayers deposited on mica in the presence of VDAC1. * indicate VBIT-4 pores and some VDAC locations are highlighted in green circles. **C. Left:** AFM image of VDAC1 after addition of 10μM VBIT-4, with a height profile showing the difference between the mica surface, VBIT-4-induced pores, and VDAC1 pores. **Right:** AFM image with a height profile highlighting the morphological differences between pores formed by VBIT-4 and those by VDAC1 pores (3). Section (1) shows a zoomed-in high resolution AFM images revealing the honeycomb-like structure of VDAC1. Section (2) is a time-lapse sequence of AFM images capturing the dynamic and the pores by VBIT-4 into the membrane (i and ii highlight the distinct morphologies of the pores induced by VDAC1 and VBIT-4). **Bottom panels: D.** The AFM image of a lipid membrane (without VDAC) on a mica substrate shown before the injection of the VBIT-4 molecule. Addition of VBIT-4 at different concentrations: 1μM **(E),** 5μM **(F),** 50μM **(G)** and 100μM **(H).** The height of the false-color scale in all images was 12 nm.

VBIT-4 partitions into lipid bilayers and induces membrane defects

The HS-AFM results prompted us to further characterize VBIT-4's membrane interaction and disruptive effects using complementary biophysical approaches. We first used microscale thermophoresis (MST), a sensitive technique for detecting molecular interactions in solution. Titration of VBIT-4 into lipid nanodiscs produced a Temperature-Related Intensity Change (TRIC) of fluorescence (Fig. 2A), yielding an average dissociation constant (K_d) of 60 μM, comparable to reported affinities of VBIT-4 for VDAC in detergent micelles[24,34]. Control experiments confirmed that this interaction was membrane-specific: 5%

DMSO alone had no effect, and MSP1D1 in the absence of lipids showed no signal change (Supplementary Fig. 2). The variability across replicates (Figure 2A and previously published titrations[24,34]) likely reflects VBIT-4's stochastic partitioning into the membrane, consistent with a lack of a specific binding site.

To evaluate the impact of VBIT-4 on membrane integrity, we used laurdan, a polarity-sensitive dye whose emission red-shifts in response to increased water penetration or lipid phase transitions. Laurdan was incorporated into PC:PE:cholesterol liposomes, which showed an emission maximum at 440 nm under baseline conditions. VBIT-4 addition led to a dose-dependent decrease in laurdan generalized polarization (GP) (Figure 2B), indicating increased water accessibility and membrane permeability (Supplementary Fig. 3). These changes were consistent with VBIT-4 partitioning into the bilayer and perturbing its structure. Taken together, these data demonstrate that VBIT-4 inserts into lipid bilayers and disrupts their physical properties in a concentration-dependent manner.

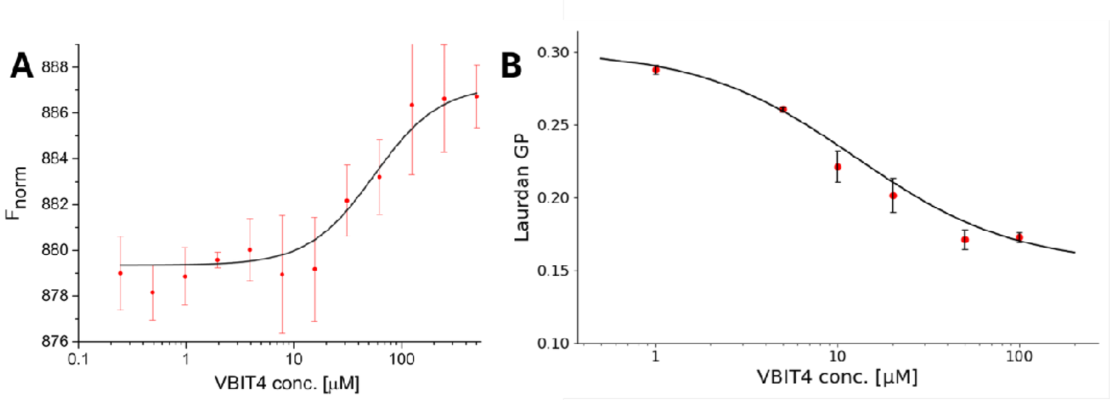

Figure 2. VBIT-4 partitions into lipid bilayers. A. MST analysis of VBIT-4 with dye labelled-MSP1D1 nanodiscs. The plot represents normalised fluorescence 650nm at a 2.5s ON-time at increasing VBIT4 concentrations. An average K_d of 60 µM was obtained. Error bars represent the standard deviations of n = 4 replicates. **B.** Laurdan GP analysis of PC:PE:Chol (62.5:30:7.5) liposomes with VBIT-4. The plot shows a VBIT-4 concentration dependent decrease in laurdan generalised polarisation of 2 biological and 4 technical replicates.

VBIT-4 induces leakage in planar lipid membranes

Having established that VBIT-4 inserts into lipid bilayers and disrupts membrane structure, we next assessed its functional impact on membrane permeability by recording transmembrane currents across planar lipid membranes (PLMs) using voltage-clamp electrophysiology. Starting from 10 µM of VBIT-4 addition to the *cis* side (grounded compartment) or both sides of the membrane, membrane conductance consistently increased with VBIT-4 concentration, inevitably resulting in membrane rupture at VBIT-4 concentrations of 20 – 50 µM (Figure 3A, B), depending on experimental conditions. VBIT-4 is a hydrophobic molecule whose membrane partitioning might depend on membrane composition. To test this, we studied the effect of VBIT-4 on PLMs of three different lipid compositions: PC/PE/Chol (60:32.5:7.5)—the same composition as was used in our AFM experiments; the soybean polar lipids extract (PLE)—lipid composition which better reflects the composition of MOM[35]; and diphytanoyl-phosphatidylcholine (DPhPC), the lipid which, to our experience, forms the most stable planar membranes. The results are summarized in Supplementary Table 1 and show that VBIT-4 essentially similarly permeabilizes phospholipid membranes of different lipid compositions, while the VBIT-4-induced conductances vary substantially even between membranes of the same lipid composition in different experiments (Figure 3C, Supplementary Table 1). In the two representative experiments shown in Figure3, membranes were formed from PC/PE/chol and PLE (Figure 3A and B, respectively). In both experiments, membrane conductance gradually increased with VBIT-4 concentration, reaching ~ 3.5 nS at 30 µM VBIT-4, in PC/PE/chol membrane

(Figure 3A) and ~5 nS at 25 μM VBIT-4 in PLE membrane (Figure 3B) before ultimately causing membrane rupture. Typically, large fast current fluctuations preceded membrane rupture as shown for both experiments in Figures 3A and 3B. Such behavior is indicative of the formation of ion-conductive, nonspecific defects or "lipidic pores" in PLM[36–38]. These structures lack discrete unitary conductance and show irregular concentration dependence, reflecting their heterogeneous amphiphile–lipid composition. Similar behavior has been reported for various amphiphilic compounds, detergents, and peptides, that typically produce noisy current traces without well-defined discrete conductance levels[39–43]. Consistent with this, VBIT-4-induced defects displayed linear (Ohmic) current-voltage relationships, symmetric across voltage polarity (insets (a) and (b) in Figures 3A and 3B), regardless of VBIT-4 addition to one or both sides of PLM. By contrast, native VDAC channels—β-barrel pores ~1.4 nm in diameter—display a well-defined conductance of ~0.7 nS under the same ionic conditions (150 mM KCl)[44]. The significantly higher and irregular conductance observed with VBIT-4 thus reflects membrane disruption, not channel activity. Therefore, our results suggest that VBIT-4 at concentrations above 20 μM potentially permeabilize cellular membranes.

In the original work by Ben-Hail *et al.*[24], where the inhibitory effect of VBIT-4 on VDAC1 oligomerization was first reported, 40 μM of VBIT-4 did not induce membrane permeabilization. However, in this work, a different method of planar membrane formation was used, producing the so-called "painted" membranes or Mueller's method, in which the lipid bilayer contains a significant amount of organic solvent, such as decane. To determine whether the difference in PLMs ("dry" membranes versus "painted" membranes) accounts for the variation in VBIT-4's effect on permeability, we conducted a series of experiments on painted membranes using the widely adopted Orbit mini system (Nanion Technologies, Munich, Germany; see Methods). Our results revealed that, starting from 5 μM, VBIT-4 consistently induced leakage in the painted planar membranes composed of DPhPC and PLE in decane (Supplementary Figure 4), mirroring its effect on "dry" membranes.

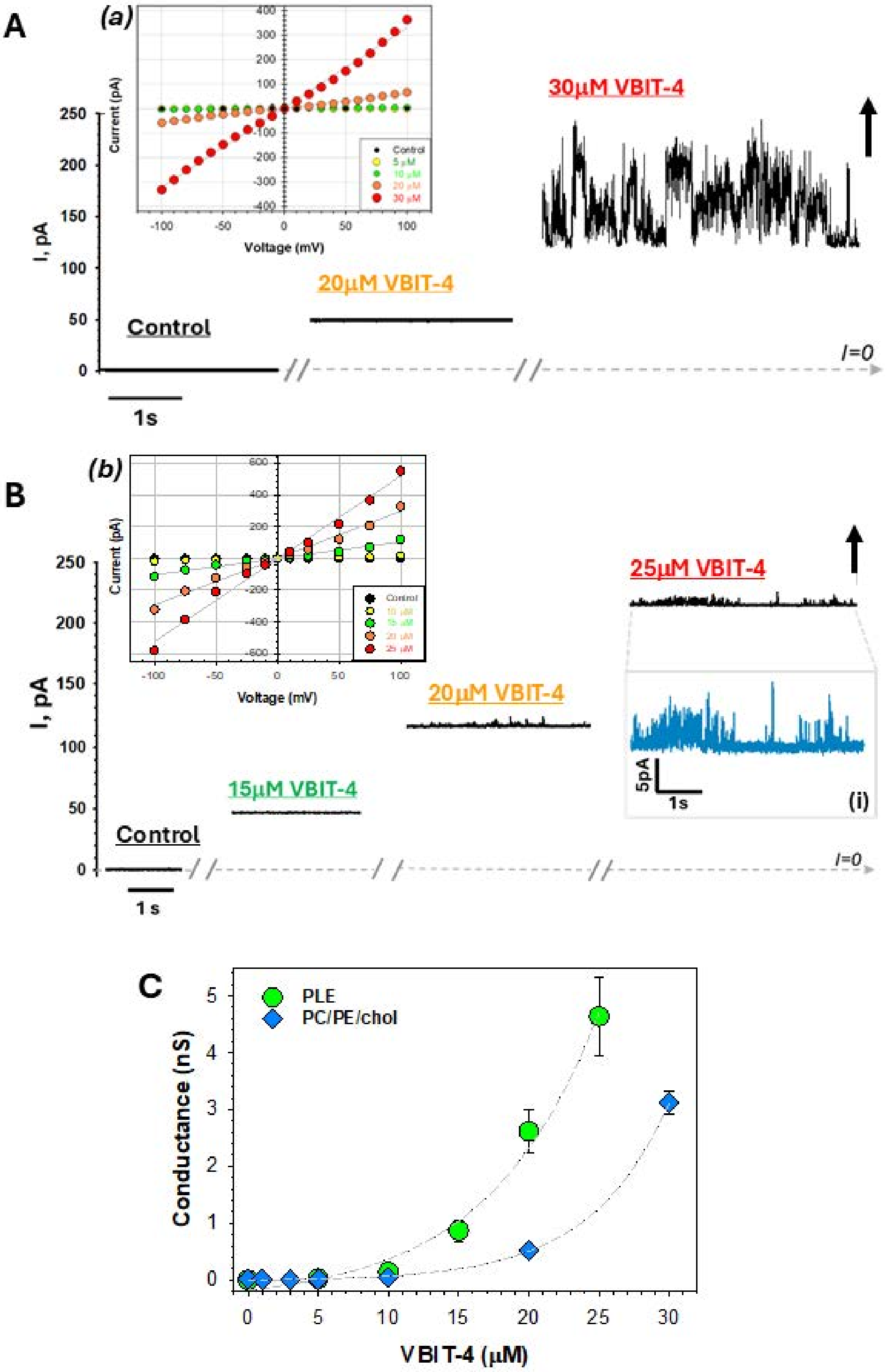

Figure 3. VBIT-4 permeabilizes planar lipid membranes. (A) Representative current traces obtained on the same PLM made from PC/PE/chol (60:32.5:7.5) before and after consequent additions of 20 and 30 µM of VBIT-4 to the *cis* compartment of the chamber at 80 mV of applied voltage. (**B**) Representative current records obtained on the PLM made from PLE before and after the addition of 15, 20, and 25 µM of VBIT-4 to both sides of the membrane at 50 mV applied voltage. Large fast fluctuations of the conductance at 30 µM (A) and 25 µM (B, inset (*i*) at the right) of VBIT-4 preceded the membrane rupture shown by upward black arrows. Inset (i) shows the current trace at 25 µM of VBIT-4 at a finer current scale. Dashed gray

lines indicate a zero current. The membrane bathing solutions consisted of 150 mM KCl buffered with 5 mM HEPES at pH 7.4. The current was digitally filtered using a 500 Hz Bessel (8-poles) filter for presentation. Insets (*a*, *b*): The current-voltage (I/V) curves obtained in experiments shown in (A) and (B), respectively, at different VBIT-4 concentrations. Gray lines are linear regressions indicating the Ohmic behavior of VBIT-4-induced conductances. (**C**) Conductance of planar membrane increases with VBIT-4 concentration. PLM were made from PC/PE/chol as in (A) and from PLE as in (B). Membrane conductance was calculated from the corresponding I/V curves. The dashed lines are exponential fit to guide the eye. Error bars are ±SD from measured conductances at different voltages.

VBIT-4 does not affect VDAC channel properties

VBIT-4 has been reported to inhibit VDAC oligomerization. To examine its effect on VDAC1 conductance and voltage gating, we performed single- and multichannel recordings in the presence of 5–30 µM VBIT-4. In contrast to Ben-Hail *et al.*[24], we observed no irreversible decrease in VDAC conductance or changes in voltage gating in eight independent experiments. Instead, VBIT-4 addition led to a dose-dependent increase in membrane conductance, as shown in the representative experiment on a single VDAC1 channel in Figure 4A. In control, VDAC1 has a typical conductance of ~4 nS in 1 M KCl. Addition of VBIT-4 led to a dose-dependent gradual increase in membrane conductance up to 6.7 nS at 30 µM VBIT-4 (Figure 4A). The observed conductance increase likely reflects a VBIT-4-induced nonspecific membrane leak**,** independent of VDAC presence, as shown in Figures 3A and 3B. Membrane rupture that follows the conductance increase, further supports this conclusion. The magnitude of the increase of membrane conductance in the presence of VDAC depended on PLM lipid composition and was on average higher in PLE than in DPhPC membranes, similar~~ly~~ to VBIT-4-induced conductance of the corresponding unmodified membranes (Figure 3).

To further investigate the nature of this additional conductance, we performed multichannel measurements. The addition of 5 µM VBIT-4 led to a slight increase in the minimum normalized conductance (G_{min}) at high potentials (Figure 4B), consistent with leakage induced by VBIT-4 observed previously (Figure 3). However, the open probability ($P_{open} = (G - G_{min}) / (G_{max} - G_{min})$), which reflects the voltage-dependent component of conductance, remained unchanged in the presence of VBIT-4. These findings show that the additional conductance induced by VBIT-4 is not voltage-gated and therefore not attributable to VDAC activity. Taken together, these results demonstrate that VBIT-4 increases membrane permeability independently of VDAC1 and does not affect VDAC's

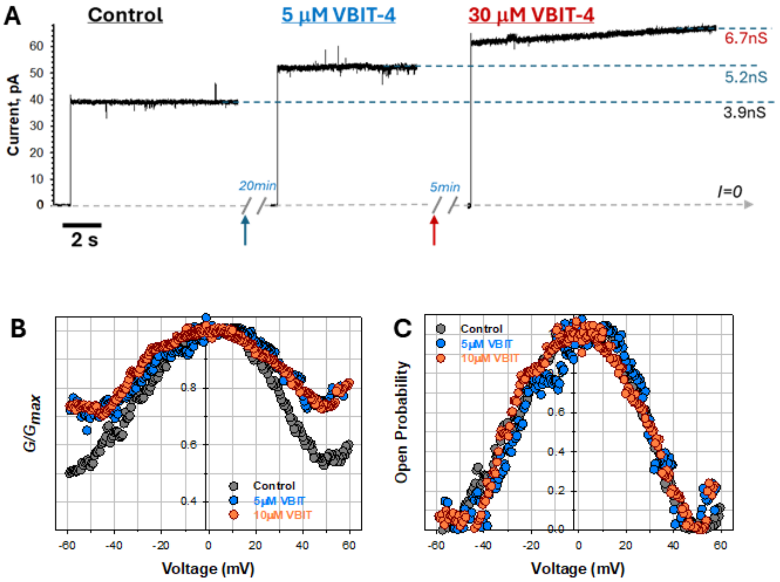

intrinsic conductance or voltage-gating properties.

Figure 4. VBIT-4 does not affect the channel properties of VDAC1. (A) Representative single-channel current traces obtained with VDAC1 reconstituted in PLM formed from PLE before (control) and after the addition of 5 and 30 µM VBIT-4 to the *cis* compartment. Addition of VBIT-4 and the time of the recordings after additions are indicated by small upward arrows. The jumps in the current correspond to the application of 10 mV voltage following the application of 0 mV. The record was obtained on the membrane with the same single channel of 4 nS conductance in the control. The gray dash line indicates zero current ($I=0$). The dashed blue lines indicate the current through the open single channel. Addition of 30 µM VBIT-4 induced a monotonic increase of membrane conductance, leading to membrane rupture. Current records were digitally filtered using an averaging time of 0.2 ms. (**B, C**) Characteristic bell-shaped plots of normalized average conductance (B) and open probability (C) as functions of the applied voltage obtained in multichannel experiment with VDAC1 in a PLE membrane in control and after addition of 5 and 10 µM VBIT-4. In all panels, the membrane bathing solutions consisted of 1 M KCl buffered with 5 mM HEPES at pH 7.4.

Mechanistic Insights into VBIT-4–Mediated Lipid Bilayer Destabilization from Coarse-Grained Simulations

Having established that VBIT-4 partitions into membranes and disrupts their integrity independently of VDAC1, we turned to MD simulations to gain mechanistic insight into its membrane interactions. MD simulations offer a powerful means to access atomic-level details of these dynamic processes, which remain challenging to capture experimentally. To access longer timescales and larger spatial dimensions, we use coarse-grained (CG) simulations, which simplify molecular representations to reduce computational cost while preserving key interactions. For this, we use the Martini 3 force field[45], a widely validated CG model known for its accuracy in simulating membrane dynamics and interactions with biomolecules, including proteins, carbohydrates, and small molecules like VBIT-4. Martini has also been extensively used to study the biophysical properties of VDAC, including its lipid interactions and membrane behavior[46,47].

The CG VBIT-4 model was parameterized from reference all-atom (AA) simulations following Martini 3 parametrization guidelines, as detailed in the methods section (Figure 5A). VBIT-4 likely exists in an equilibrium between its neutral and protonated states; since each adopts distinct conformations, we developed separate Martini CG models to analyze their effects individually (see Methods for details). Although both states likely coexist in vivo, accurately capturing this equilibrium computationally remains challenging.

VBIT-4 readily inserts into lipid bilayers

Unbiased MD simulations of a single VBIT-4 in water show that it readily inserts into lipid bilayers, consistent with its hydrophobic character (Figure 5D,E), a behavior well captured by the Martini 3 forcefield. The $\log P_{(oct/water)}$ scale measures a molecule's hydrophobicity, with values below 0 indicating polar, water-soluble molecules (e.g., glucose, logP ~ -3.2[48]), and values above 0 indicating apolar, lipophilic molecules (e.g., cholesterol, logP > ~ 8[49]). A predicted logP of ~3.5 places VBIT-4 in the moderately hydrophobic range (Figure 5E), similar to ibuprofen (logP ~ 3.9[50]), meaning it readily partitions into lipid membranes. Consistent with this, unbiased simulations of VBIT-4 in water show that it readily self-aggregates into micelle-like clusters or aggregates, regardless of its charge state (Supplementary Figure 1).

To determine whether VBIT-4 can translocate across biological membranes—which is expected in cells to reach the mitochondrial membranes—we performed umbrella sampling simulations to compute the Potential of Mean Force (PMF), which quantifies the free energy profile along the translocation pathway. As expected, the neutral form of VBIT-4 has a significantly lower translocation barrier (~30 kJ/mol) compared to the charged form (~55 kJ/mol, Figure 5C). Although we anticipate VBIT-4 to be predominantly deprotonated when deeply inserted into the hydrophobic region of membranes, the translocation barrier remains relatively high. While this level of resistance may reduce the frequency of spontaneous permeation events, it is still compatible with passive translocation under physiological conditions. The process could be further facilitated by several factors such as membrane defects or transient pore formation — especially under conditions of elevated local VBIT-4 concentration — which are known to lower local energetic barriers. These effects may enhance the likelihood of translocation events in a cellular context. It is important to note that the energy barrier estimated here applies to a single VBIT-4 molecule and does not account for cooperative or concentration-dependent effects. Overall, these CG-MD simulations show that VBIT-4 not only partitions into the membrane but also has the potential to translocate across it.

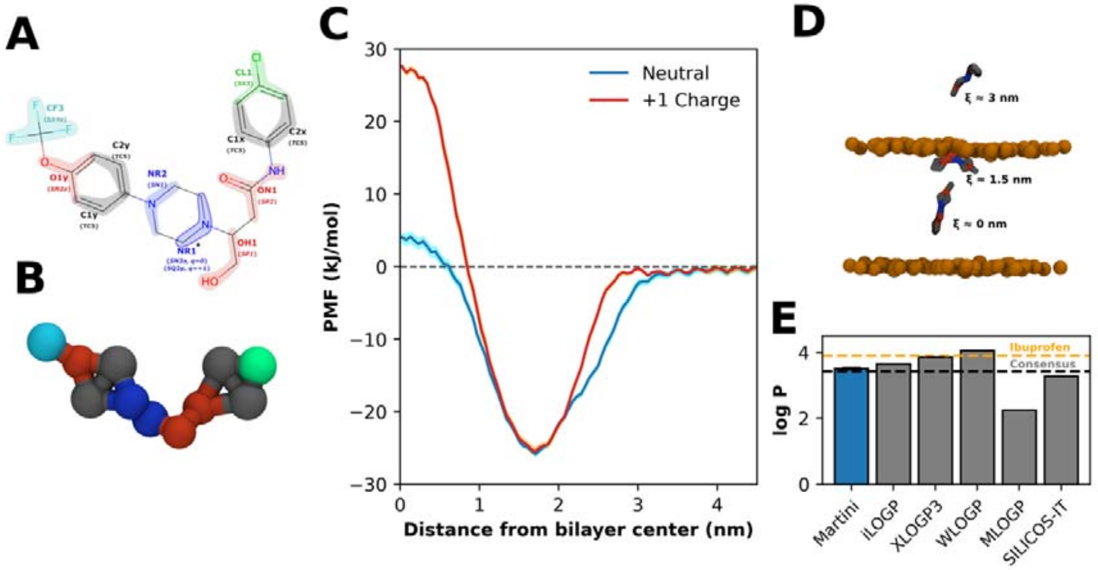

Figure 5. VBIT-4 is a hydrophobic molecule that can partition and cross membranes. (A) VBIT-4 Chemical structure and Martini 3 model mapping. Atom-to-bead mappings are indicated by the coloured shapes. Assigned Martini 3 bead names are indicated for each bead as overlaid bold text, with the corresponding bead types in italic text. Protonable group is highlighted (⋆). (B) VBIT-4 Martini 3 CG model. (C) Potential Mean Force (PMF) of VBIT-4 insertion into coarse-grained MOM membranes. Free energy profiles are shown for both the neutral (blue) and protonated (+1 charge, red) forms of VBIT-4. (D) Snapshots of the insertion of neutral VBIT-4 at different distances from the bilayer center (ξ); lipid PO_4 beads are represented in orange, and VBIT-4 in grey/red/blue. (E) Predicted octanol–water partition coefficient (Log□P) values for VBIT-4. VBIT-4 hydrophobicity was estimated using several computational predictors (gray) and the Martini 3 coarse-grained model developed in this study (blue). Higher Log□P values indicate greater lipid solubility. The dashed black line shows the consensus value across predictors, while the orange dashed line marks the Log□P of ibuprofen (~3.9), a well-known hydrophobic drug used here for comparison.

VBIT-4 partitions into lipid membranes and induces membrane destabilization

To test the impact of VBIT-4 on the biophysical properties of lipid membranes, we simulated a MOM mimic membrane at increasing VBIT-4 concentrations (ranging from 1:16 to 1:1.5 VBIT-4-to-lipid ratio), in both charged (Figure 6A) and neutral forms (Figure 6B). VBIT-4 molecules were initially placed in the solvent and subsequently inserted into the membrane during equilibration, with equal distribution across both leaflets. For each condition, 3 replicas of at least 10□μs were simulated. We then analyzed general membrane biophysical properties—such as area per lipid, bilayer thickness, and lipid order—as well as indicators of membrane integrity, including water permeation (leakiness), lipid flip-flop (loss of asymmetry), and tail protrusion (packing defects). Notably, the CG-Martini force field is known to overstabilize membranes as evidenced by the dramatic underestimation of polar defect formation in Martini[51], suggesting that any observed destabilizing effects likely underestimate the actual impact on biological membranes.

At lower VBIT-4-to-lipid ratios (<1:3), the insertion of both neutral and protonated VBIT-4 increases the area per lipid (APL) (Figure 7A) — the average surface area occupied by each lipid in the membrane plane — and decreases both membrane thickness (Figure 7B) and lipid order (Figure 7C). A significant rise in membrane water permeability is also observed (Fig. 7E). However, no notable membrane undulations or defects indicative of major membrane disruption are detected.

At higher VBIT-4-to-lipid ratios (>1:3), the behavior of the neutral and protonated forms of VBIT-4 diverges. Neutral VBIT-4, upon reaching a critical concentration, aggregates significantly, forming a pore-like structure in the membrane. The core of the pore is mostly dry, with only a few water beads being pulled in, but no distinct water channel forms. This is evident from the stabilization of water-crossing events observed at neutral pH (Figure 7E). However, this formation causes a significant number of lipids to be drawn toward the center of the bilayer , inducing extensive lipid flip-flop (Figure 7F)and lipid tail protrusion events (Figure 7D). In contrast, charged VBIT-4 does not spontaneously form this pore-like structure; instead, at high concentrations, it induces a dramatic increase in membrane water permeability (Figure 7E).

These simulations are influenced by two limitations: (i) the charge state of VBIT-4 and (ii) the overestimation of lipid bilayer stability in Martini. Given that the pKa of the piperazine group is close to physiological pH, VBIT-4 is unlikely to exist solely in a fully charged or fully neutral state. Instead, its charge state will depend on the surrounding environment—likely neutral when deeply inserted into the membrane and charged when near the phosphodiester/glycerol region. Therefore, the observed behavior is likely a combination of both charge states. If a pore-like structure forms upon reaching a critical concentration, it is probable that while the outermost layer of deeply inserted VBIT-4 molecules remains neutral, those near the PO_4 layers and potentially within the pore core may be charged, facilitating the formation of water defects. To better approximate a realistic scenario, we also simulated a 50:50 mixture of charged and neutral VBIT-4 molecules. These simulations still showed aggregation and the formation of structures, similar to those observed with neutral VBIT-4, while exhibiting membrane behavior intermediate between the fully charged and fully neutral conditions (Supplementary Figure 5). Since Martini is known to over-stabilize lipid bilayers, while in these simulations we do not observe definitive signs of VBIT-4 induced water-permeable pores, the structures formed by phase-separation at high concentrations of neutral VBIT-4 likely represent the observed defects reported in AFM and electrophysiology.

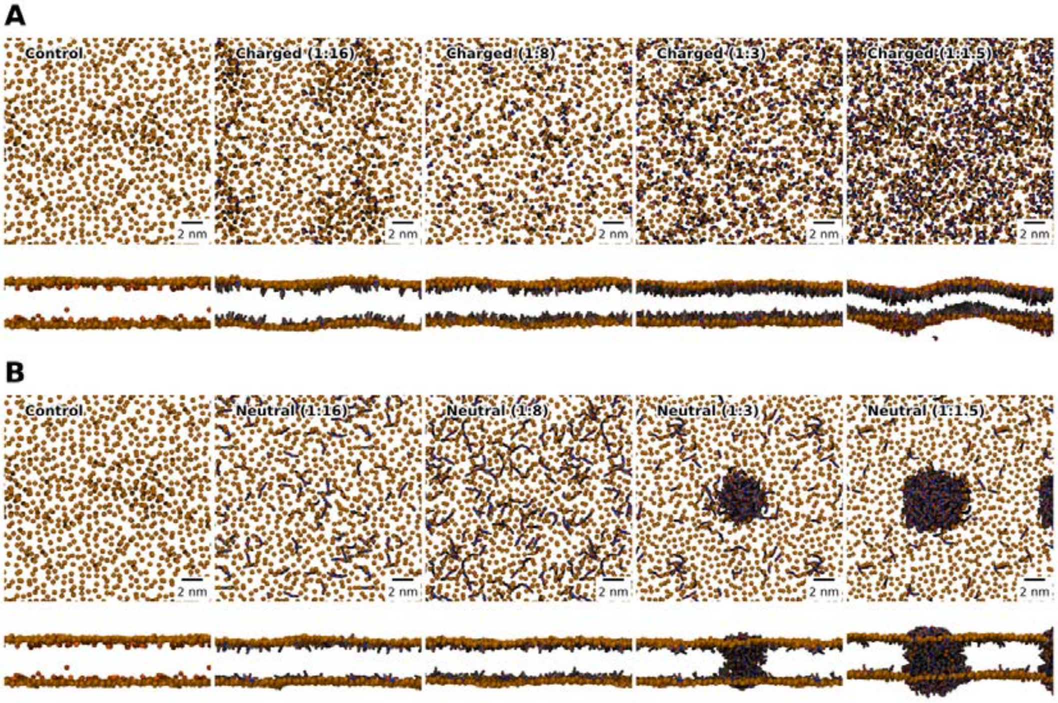

Figure 6. VBIT-4 forms pore-like structures through phase separation. Representative snapshots showing the impact of increasing VBIT-4 concentrations on MOM membrane mimics after 10 µs of CG MD simulation. (Lipid phosphate beads are shown in orange; VBIT in grey, with chemically distinct beads highlighted in red and blue). Top and side snapshots are shown for both charged (A) and neutral (B) VBIT-4 forms at increasing VBIT:Lipid ratios (0, 1:16, 1:8, 1:3, 1:1.5).

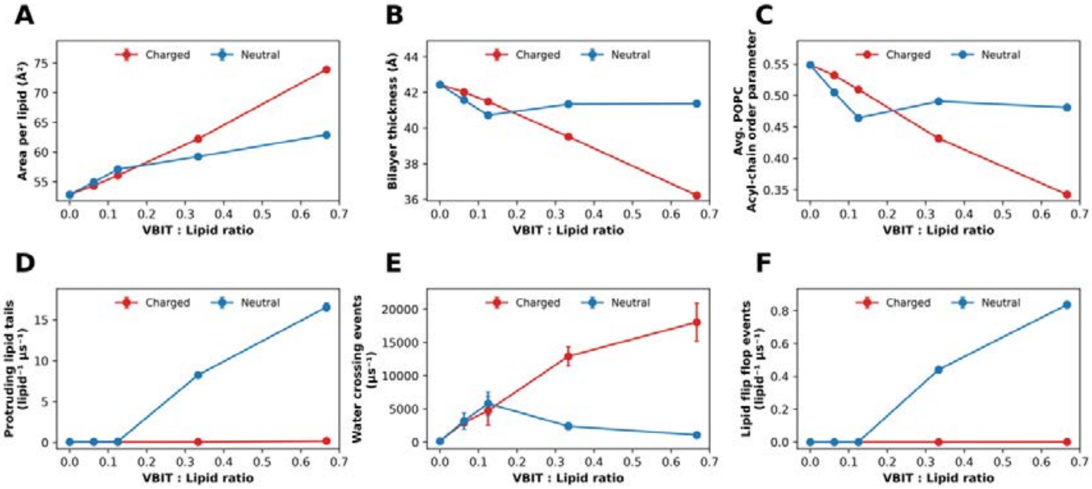

Figure 7. VBIT-4 disrupts membrane stability in a concentration-dependent manner. Lipid biophysical properties of MOM mimic membranes were evaluated in the presence of increasing VBIT-4 concentrations, either in the charged (red) or neutral (blue) form. We monitored several indicators of membrane integrity: (A) Area per lipid, (B) Bilayer thickness and (C) POPC acyl-chain order (membrane packing and organization); (D) Lipid tail protrusion (packing defects); (E) Bilayer water crossing (membrane permeability); and (F) Lipid flip-flop (bilayer asymmetry). Each system was

simulated for 10 µs in triplicate, and error bars represent the standard deviation across replicas.Data for the 50:50 charged:neutral mixed form are displayed in Supplementary Figure 6.

VBIT-4 facilitates the formation of polar defects in lipid bilayers

To clarify the role of VBIT-4 in the stability of lipid bilayers, we examined its impact on the energy required to induce polar defects. Polar defects in lipid bilayers occur when water molecules and polar lipid headgroups penetrate the hydrophobic core of the membrane. The energy required to form such defects determines membrane stability, with higher barriers preventing disruption and lower barriers making the membrane more susceptible to perturbation. To this end, we utilized the pore-formation reaction coordinate developed by Jochen Hub and applied umbrella sampling to probe this effect[52]. The Martini 3 force field has been shown to overestimate the energy barriers for polar defect formation in reference membranes by more than 200 kJ/mol. Therefore, as expected, the Potential of Mean Force (PMF) calculated for the control system (without VBIT-4) reveals a high barrier of approximately 250 kJ/mol for polar defect formation. In comparison, all-atom simulations of DPPC membranes typically show much lower barriers around 50 kJ/mol, with a metastable pore forming when the reaction coordinate (ξ) reaches near 1. This significant difference of approximately 200 kJ/mol can be attributed to the stabilizing effects of the Martini 3 force field, which artificially increases the barrier for defect formation compared to all-atom simulations.

When comparing the PMF for both charged and neutral VBIT-4 molecules at a ~1:3 VBIT-to-lipid ratio to the control system without VBIT-4 (Figure 8A), we observe a decrease of approximately 60 and 100 kJ/mol, respectively, in the energy required to induce polar defect formation in the membrane. Although these barriers, around 150 kJ/mol, are still too high for spontaneous defect formation in Martini, it is important to note that the Martini 3 force field overestimates these barriers by more than 200 kJ/mol in reference membranes. Therefore, these results suggest that VBIT-4 can destabilize lipid bilayers and promote the formation of polar defects (Figure 8B). One limitation of these simulations is that the small system size used in the umbrella sampling does not allow for a sufficient number of VBIT-4 molecules to fully assemble into the pore-like structures seen in larger unbiased MD simulations. In larger systems, where VBIT-4 concentrations are higher, the barrier for polar defect formation may be further reduced.

Consistent with these findings, our unbiased MD simulations also reveal clear changes in membrane biophysical properties—including increased area per lipid, reduced thickness, enhanced water permeability, and more frequent lipid tail protrusions and flip-flop events—all of which indicate reduced membrane integrity with increasing VBIT-4 concentrations and support the formation of bilayer defects, in agreement with the polar defect formation PMF profiles.

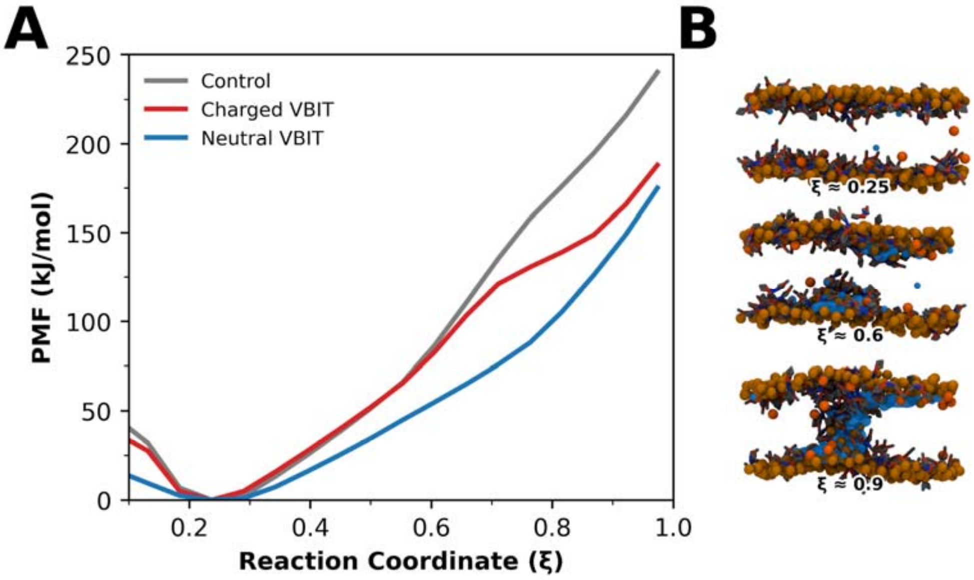

Figure 8. VBIT-4 facilitates the formation of polar defects in model membranes. (A) Potential Mean Force (PMF) profiles for polar defect formation in coarse-grained MOM membrane systems, shown as a function of the pore formation reaction coordinate ξ, for membranes without VBIT-4 (grey), with charged VBIT-4 (red), and with neutral VBIT-4 (blue). Curve uncertainty (in the single-digit kJ mol^{-1} range) is represented by shading in the same colours along the corresponding curve (for some points at the edges of the reaction coordinate range, an error could not be estimated). (B) Representative snapshots of the membrane systems in the presence of neutral VBIT along the reaction coordinate; lipid PO_4 beads are represented in orange, cholesterol ROH in dark orange, water beads in blue (only those in the vicinity of the lipid headgroups or the established defect are represented), and VBIT-4 in grey.

VBIT-4 increases membrane permeability and cytotoxicity in HeLa cells

Given the membrane-disrupting effects of VBIT-4, its partitioning into membranes could potentially contribute to cellular cytotoxicity. We assessed its cytotoxicity in live cells using a fluorescence-based assay that reports on both membrane integrity and cell death. This dual measurement approach provides a comprehensive evaluation of the cytotoxic effects of VBIT-4, allowing us to directly correlate membrane disruption with cellular damage. An IC_{50} of 25.91 ± 3.55 µM and 29.84 ± 2.68 µM was calculated for VBIT-4 from the fluorescence data for cell viability and cytotoxicity, respectively (Figure 9). Notably, the VDAC1 knockout (KO) did not affect the IC_{50} values (Supplementary Figure 7), suggesting that the action of VBIT-4 on HeLa cells is independent of VDAC1.

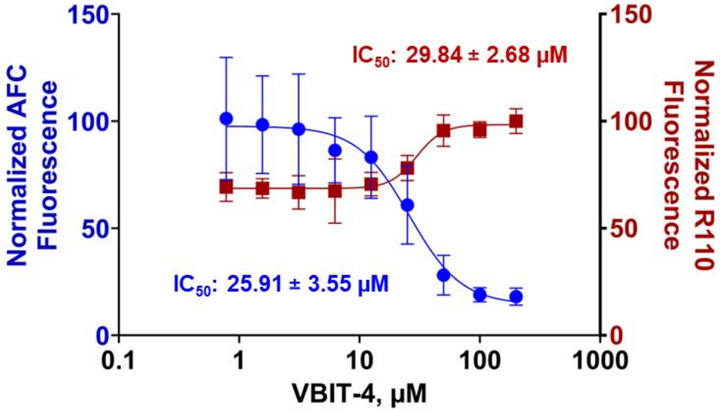

Figure 9. VBIT-4 decreases viability and increases cytotoxicity in HeLa cells. Graph representing the decrease in cell viability (**blue**) and increase in cytotoxicity (**red**) with increasing concentration of VBIT-4 measured using GF-AFC and bis-AAF-R110, respectively. Data normalized to the maximum fluorescence from three independent experiments with 3-4 repeats each were included for the fitting, and the error bars represent the standard deviation.

Discussion

VBIT-4 was introduced in 2016 as an inhibitor of VDAC1 oligomerization, proposed to directly bind VDAC1 and prevent oligomerization and apoptosis in cells treated with selenite and cisplatin[24]. Since then, VBIT-4 has been widely used to investigate VDAC oligomerization in various cellular pathways and disease models (e.g., lupus-like disease[11], ALS[26], Alzheimer’s disease[28], epileptic seizure[53]). Despite its broad use, the molecular mechanism of VBIT-4 remains unclear, and its specificity for VDAC1 oligomers has generally been accepted without thorough validation. Given its widespread applications, a detailed understanding of VBIT-4’s mode of action is essential.

Our study shows that VBIT-4 primarily partitions into lipid membranes rather than binding directly to VDAC1. Using AFM, we visualized VBIT-4 localizing to protein-free lipid regions and disrupting bilayer integrity without altering VDAC1 clusters. This conclusion is supported by microscale thermophoresis, which showed that VBIT-4 partitions into lipid nanodiscs in the absence of VDAC, with affinities comparable to those reported for VDAC in detergent micelles[24,34]. Laurdan-based polarity measurements further confirmed both membrane insertion and perturbation, showing a dose-dependent decrease in generalized polarization consistent with increased water penetration and lipid disorder, and yielding a membrane partition coefficient characteristic of a hydrophobic compound. Importantly, VBIT-4 not only inserts into bilayers but also disrupts their structure: our MD simulations show that it induces lipid flip-flop, increases area-per-lipid, reduces bilayer thickness, and promotes water permeation and tail protrusion. At higher concentrations, it drives lateral phase separation and the formation of pore-like defects. These findings were corroborated by electrophysiological recordings, which demonstrated that VBIT-4 causes membrane permeabilization in a concentration-dependent manner, becoming prominent around 20 μM—within the range commonly used in both in vitro and cellular assays[24,26,28,54]. These findings reveal that VBIT-4 acts as a membrane-active compound, underscoring the importance of including lipid-only controls when evaluating small molecules targeting membrane proteins, as their hydrophobic nature can lead to membrane destabilization.

Despite its involvement in multiple pathological pathways, VDAC is a challenging therapeutic target due to its central role in mitochondrial physiology and the absence of a well-defined catalytic cleft[20]. VDAC oligomerization, although implicated in key cellular processes—including lipid scrambling[12], mitochondrial organization[21], apoptosis[55,56], and interaction with cytosolic[46,57,58] and MOM proteins[22]—is also a poor target. Except for a few defined dimeric interfaces involved in specific processes (e.g., e.g., β17-19–β1-3 lipid scrambling[12] or β4–β6 pH sensing[59]), VDAC does not form discrete oligomers with stable protein–protein interfaces. Instead, it assembles into heterogeneous lipid–protein clusters[1,2,23], whose size and compaction are tightly regulated by the surrounding lipid environment[23]. This lipid dependence introduces inherent variability, making selective disruption of VDAC “oligomerization” both conceptually and technically problematic.

Our data demonstrate that VBIT-4 is not a specific VDAC inhibitor but rather a membrane-perturbing agent that indirectly alters VDAC clustering. AFM imaging showed that VBIT-4 partitions into lipid-rich, protein-free regions, and our biophysical and simulation data confirmed that it disrupts bilayer integrity. The impact of VBIT-4 on VDAC “oligomers” or clusters is generally investigated by cross-linking and SDS-PAGE. Since VDAC clustering is highly sensitive to bilayer composition[23], even subcytotoxic concentrations of VBIT-4 could alter lipid packing and shift the balance between more compact and lipid-rich clusters. Such changes would directly influence VDAC cross-linking, which is the primary method used in several studies to assess VDAC oligomerization[11,24,60,61]. These changes likely account for the reduced VDAC cross-linking observed in VBIT-4–treated cells[11,24], as cross-linking requires direct protein–protein contact, which is lost in lipid-expanded clusters. Importantly, while such reorganization may affect VDAC's interaction with partners like hexokinase, Bak, or Bax, it does not imply specific inhibition of VDAC oligomerization.

The proposed membrane-centric mechanism of action implies that VBIT-4 may affect numerous membrane-bound pathways beyond VDAC. Because membrane lipids critically govern protein localization, clustering, and function, nonspecific perturbation of bilayer structure—such as that induced by VBIT-4—can trigger diverse cellular responses. As such, attributing the cellular phenotypes observed in VBIT-4–treated cells solely to inhibition of VDAC oligomerization is unwarranted. VBIT-4's broad activity underscores the need to incorporate lipid-based controls when evaluating candidate drugs targeting membrane proteins.

More generally, membrane-active compounds pose distinct challenges for drug development. Lipid environments vary widely across organelles and cell types, complicating the prediction of drug distribution, efficacy, and toxicity. Drugs such as licofelone—a dual COX/5-LOX inhibitor—failed in clinical trials in part due to off-target membrane effects[62], while others like omeprazole intercalate into DPPC membranes and modulate lipid domains[63]. These cases exemplify how membrane interactions, if not properly accounted for, can obscure our understanding of drug action. Incorporating analyses of drug–membrane interactions into early-stage development may therefore enhance both mechanistic insight and clinical translatability.

Toxicity assays in wild-type and VDAC1 knockout HeLa cells revealed increased cell death at concentrations >10 µM, consistent with previous reports by Belosludtsev et al.[64], who observed cytotoxicity above 15 µM. Notably, the authors suggested that the observed in their experiments on isolated mitochondria Ca^{2+} retention capacity decrease at 30 µM VBIT-4 may indicate that VBIT-4 is a mitochondrial pore inducer. The membrane defects and pore formation seen across our in vitro systems likely underlie this toxicity. Upon cellular exposure, VBIT-4 is expected to first partition into the plasma membrane and then redistribute across intracellular membranes—including those of the ER, Golgi, mitochondria, and other organelles—based on its hydrophobicity and lipid affinity. Its intracellular accumulation is further influenced by membrane potential; as a lipophilic cation, VBIT-4 may concentrate in polarized compartments by Nernstian behavior, akin to dyes like TPP, TMRM, or MitoSOX[65]. Supporting this, Belosludtsev et al.[64] detected VBIT-4 in the mitochondrial inner membrane, where it inhibited respiratory complexes I, III, and IV, reinforcing its broad, non-specific membrane activity.

In contrast, Oflaz et al.[61] reported no increase in cell death at 20 µM. This discrepancy may reflect differences in assay sensitivity, cell lines, modes of compound delivery, or the stability of VBIT-4. Notably, the compound is hydrophobic and chemically unstable, reportedly degrading within a month at –20 °C in DMSO (Selleckchem datasheet), which could significantly impact its bioactivity. Furthermore, most published studies used VBIT-4 at concentrations between 10-20 µM, which may avoid overt cytotoxicity but not necessarily prevent membrane perturbation or other VDAC-independent effects.

In several disease models—including ALS[26], lupus[11], and apoptosis[24,61]—VBIT-4 has been reported to rescue cell viability. However, pathological states often involve altered membrane composition and protein expression, and VBIT-4 may counteract some of these changes by modulating membrane properties. Given that its precise mechanism at the membrane level in vivo remains poorly defined, these protective effects cannot be straightforwardly attributed to the inhibition of VDAC oligomerization and should be interpreted with caution.

Conclusions:

Although VBIT-4 was developed and widely used as a VDAC1 oligomerization inhibitor, its precise mechanism of action remained uncharacterized. Our findings challenge its specificity, demonstrating that VBIT-4 disrupts membrane integrity by integrating into lipid bilayers, altering lipid organization, and inducing permeabilization independently of VDAC. These membrane-centric effects raise significant concerns about its off-target action, indicating that VBIT-4 is unsuitable for probing VDAC oligomerization or related pathways. Conclusions from previous studies employing VBIT-4 should therefore be re-evaluated. While our study focused on VBIT-4, similar membrane-disruptive properties are likely to extend to related compounds such as VBIT-3, VBIT-12, and NSC15364[24,60].

Acknowledgements

We thank Dr. Manuel N. Melo for the insightful suggestion that inspired the polar defect formation simulations. This work was supported by the Aix-Marseille Université grant AMX-21-PEP-022 (L.B.) and a PhD fellowship from Aix-Marseille Université (V.R.). L.B.A. acknowledges the support of the French National Centre for Scientific Research and the HPC resources provided by IDRIS, CINES, and TGCC through GENCI (allocation 2024-A0160713456). L.B.A. also acknowledges the support of the Centre Blaise Pascal de Simulation et Modélisation Numérique's IT test platform at ENS de Lyon (Lyon, France) for the computer facilities. M.S.W., N.A.B., B.G.B., M.G.L., M.R., S.M.B., and T.K.R. acknowledge the support of the Intramural Research Program of the National Institutes of Health (NIH), *Eunice Kennedy Shriver* National Institute of Child Health and Human Development (NICHD).

Methods:

mVDAC1 purification:

mVDAC1 production and purification was described in details in [66].

AFM and HS-AFM data acquisition

To form a homogeneous protein containing supported lipid bilayer (SLB), a mixture of 15 µl of the proteoliposome suspension (1 mg/ml) and 85 µl of "Incubation buffer" (10 mM HEPES pH 7.4, 100 mM NaCl, 15 mM CaCl2) was incubated 1 hour at room temperature on a freshly cleaved mica under a humid hood. The sample was rinsed 10 times in ultrapure water (MilliQ) and imaged by AFM/HS-AFM in "Imaging buffer" (10 mM HEPES pH 7.4, 100 mM NaCl, 5 mM CaCl2) at 35 °C to check the homogeneity of the formed membrane. All conditions have been performed in triplicates.

Conventional AFM imaging was performed in contact mode with a Nanoscope IIIe Multimode AFM (Bruker, Santa Barbara, CA, USA) using OTR4 probes of k=0.1 N/m. The scan rate, gains and deflection setpoint were adjusted during acquisition to optimise the quality of acquired images.

HS-AFM movies were acquired in amplitude modulation mode optimized high–resolution imaging parameters with a modified HS-AFM (SS-NEX, RIBM, Tsukuba, Japan)[67]. The apparatus is equipped with our custom-made digital high-speed lock-in amplifier coded on a reconfigurable FPGA using LabView (National Instruments, Austin, USA). Short cantilevers (length ~7 µm) designed for HS-AFM, presenting an electron beam deposition (EBD) tip, were used (USC-F1.2-k0.15 Nanoword, Switzerland). They are characterized by a nominal spring constant k = 0.15 N/m, a resonance frequency in liquid of 500 kHz, and a quality factor Qc ~ 2 (in liquid). HS-AFM sensitivity to probe the deflection was 0.1 V/nm. The imaging amplitude setpoint was set to ~90% of the free amplitude (~10 Å). All experiments were performed at 35 °C, by introducing the HS-AFM microscope into a temperature-controlled box.

Image analysis

Acquired images were plane-fit and flattened using the AFM processing and analysis software provided by the instrument manufacturer. HS AFM image treatment was limited to the correction of

XY drift and a first-order X-line fit. Image analysis was performed using the general distribution of ImageJ[68] and of WSxM[69].

Preparation of nanodiscs

MSP1D1 membrane scaffold protein was produced and purified as described by Ritchie, T. K. et al.[70]. Chloroform-solubilised lipids (Chicken egg phosphatidylcholine) were dried under nitrogen gas and re-solubilised in 20 mM Tris pH 8.0 buffer containing 50mM sodium cholate at a final concentration of 25 mM lipid. Lipids and MSP were mixed at a 65:1 molar ratio at 4°C for 1 hour. Bio-Beads SM2 were added at a 10x excess (weight) of total detergent, and the mix was incubated overnight at 4 °C on agitation. The nanodiscs were filtered through a 0.2 µm sterile syringe filter and centrifuged at 100,000 x g for 30 minutes at 4 °C. The supernatant was subjected to size exclusion chromatography on a Superdex 200 increase 10/300 GL column in 20 mM HEPES pH 7.4, 100 mM NaCl. The nanodisc-containing fractions were concentrated and labelled as described in the MST experiments.

Microscale Thermophoresis (MST) experiments

MST experiments were performed using a NanoTemper Monolith NT.115. Briefly, MSP1D1 lipid nanodiscs were labelled using the Protein Labelling Kit RED-NHS 2nd Generation from NanoTemper (NT-L021) at a 1:1.5 protein:dye molar ratio in 20 mM HEPES buffer pH 7.4, 100 mM NaCl for 2 hours at 4°C in the dark. Excess dye was removed using a Micro Bio-Spin P6 column equilibrated in the same buffer. The degree of labelling was determined using UV-Vis spectrophotometry at 650 nm and 280 nm according to the manufacturer's instructions. The degree of labelling was between 0.6-0.75 ($\varepsilon_{nanodisc}$ = 36,900 M^{-1} cm^{-1}, ε_{dye} = 195,000 M^{-1} cm^{-1}) across the replicates. VBIT-4 (Selleckchem #S3544) was dissolved in DMSO at a concentration of 10 mM and sub-stocks of 1 mM were made in buffer containing 10 % DMSO. 15 µL of labelled nanodiscs were incubated with 15 µL of VBIT-4 (0.25 - 500 µM) and incubated for 20 minutes at room temperature as performed by Ben-Hail et. al.[23]. Following a short spin at 10,000 x g, 10 µL of the samples were loaded into 12 glass capillaries (NanoTemper premium capillaries, MO-K022) and thermophoresis was performed (60% excitation power, medium MST power). The final concentration of DMSO in the capillaries was maintained at 5%. Thermophoresis experiments were performed as described by the manufacturer and data were analysed at 650 nm at a laser ON-time of 2.5s. Data were fitted by the system for n=4 replicates.

Laurdan generalised polarisation experiments:

Laurdan-containing liposomes were prepared by mixing chloroform-solubilised lipids (PC:PE:Chol, 62.5:30:7.5) at a concentration of 1 mM total lipids with chloroform-solubilised laurdan at a lipid:laurdan molar ratio of 1:1000. Lipid mixtures were dried under nitrogen gas in the dark. Liposomes were formed by resuspending dried lipids in 200 µL of 20 mM HEPES buffer pH 7.4 containing 100 mM NaCl and vortexing. Liposomes were sonicated with 10 pulses at 10% power, 10% ON/OFF cycle to form SUVs of diameter 50 nm or 100 nm as verified by dynamic light scattering. Laurdan-containing liposomes were diluted 10x in buffer and added to a quartz cuvette (pathlength 3 mm) at a final volume of 150 µL. Sub-stocks of VBIT-4 in DMSO were made such that the final volume added to the cuvette would be a constant 0.6 µL. Control samples contained the same volume of DMSO. The excitation wavelength was set to 375 nm and the emission scan range was from 400-600 nm. Excitation slit width - 10nm, emission slit width - 5nm. Data were recorded at a scanning speed of 600 nm/min at 26 °C on a Cary Eclipse fluorescence spectrometer.
Generalised polarisation was calculated as $GP = (I_{440} - I_{490}) / (I_{440} + I_{490})$. GP was plotted as a function of VBIT-4 concentration on Python using a partitioning model, and the partitioning coefficient (K_p) was calculated from the equation $y = F_{min} + (F_{max} - F_{min}) / (1 + K_p * x)$.

Planar lipid bilayer measurements

Planar lipid membranes (PLM) were formed by two different techniques: 1) using "dry" membranes formed by the lipid monolayer opposition technique on a circular aperture in a Teflon partition dividing two ~1.5 mL (*cis* and *trans*) compartments of the experimental chamber, as previously described[71], and 2) using "painted" membranes from lipid solution in decane using Orbit mini system (Nanion Technologies, Minich, Germany)[72]. Lipids dioleoyl-phosphatidylcholine (DOPC), dioleoyl-phosphatidylethanolamine (DOPE), diphytanoyl-phosphatidylcholine (DPhPC), polar lipid extract from soybean (PLE), and cholesterol (Avanti Polar Lipids) were used for PLM preparations. Aqueous solutions consisted of 150 mM KCl buffered with 5 mM HEPES at pH 7.4. In the first method of PLM formation, the 5 mg/mL lipid mixtures in pentane were used. The aperture in the Teflon partition was pretreated by 1% hexadecane in pentane before PLM formation, thus leaving only a residual amount of hexadecane in the bilayers. The current recordings were performed as described previously[71], using Axopatch 200B amplifier (Axon Instruments) in the voltage-clamp mode. Data were filtered by a low-pass 8-pole Butterworth filter (Model 900 Frequency Active Filter, Frequency Devices) at 15 kHz, digitized with a sampling frequency of 50 kHz, and analysed using pClamp 10.7 software (Axon Instrument). For data analysis, digital filtering using a 1 or 0.5 kHz low-pass Bessel filter was applied. Potential is defined as positive when it is greater on the *cis* side, the side of VBIT-4 and VDAC1 addition. In the second method, lipid bilayers were formed by painting the chips (Ionera, Freiburg, Germany) with the 5 mg/mL lipid mixtures in decane. Multi Electrode Cavity Array (MECA4) chips were filled with 150 µL of 150 mM KCl solution at pH 7.4. VBIT-4 in DMSO solution was added to the bilayer in both experimental setups after PLM was formed, and its conductance of less than 0.1 pS was verified. All measurements were performed at room temperature of 21 ± 1°C.

VDAC conductance measurements

Recombinant mouse VDAC1 was expressed, refolded, and purified as described previously[73]. Channel insertion was achieved by adding 0.1-1.5 µL of VDAC diluted in buffer containing 10 mM Tris, 50 mM KCl, 1 mM EDTA, 15 % (v/v) DMSO, 2.5% (v/v) Triton X-100, pH 7.0. Current recording and its analysis were performed as described previously[74]. VDAC voltage-gating properties were assessed following the previously described protocol [75] under the application of a slow symmetrical 5 mHz triangular voltage wave of ±60 mV amplitude from an Arbitrary Waveform Generator 33220A (Agilent). Data were acquired at a sampling frequency of 2 Hz and analyzed as described previously[75] using an algorithm developed in-house and pClamp 10.7 software. In each experiment, current records were collected from membranes containing 10-50 channels in response to 5–10 periods of voltage waves to ensure data collection from more than 50 channels per experiment. Only the part of the wave, during which the channels were reopening, was used for the subsequent analysis[76].

VBIT-4 CG parameterization.

VBIT-4 charge state. VBIT-4 contains a piperazine group with two nitrogen atoms. These are typically protonable under physiological conditions, with pKa values usually in the range of 7–9. Out of these two, the most protonable nitrogen is the one closer to the hydroxyl (-OH) and amide (-CONH-) groups. The nitrogen near the benzene ring is both sterically hindered and electronically less basic due to the $-OCF_3$ group's electron-withdrawing effect. The nitrogen near the amide and hydroxyl is both more exposed and more basic, making it the preferred protonation site. Given the significant conformational differences observed between the neutral and protonated versions of VBIT-4 in our reference AA simulations, we developed a Martini CG model for each state and analyzed their effects separately.

All-atom reference simulations. VBIT-4 Martini 3 models were based on simulations of all-atom counterparts, parameterized using the OPLS-AA force field via LigParGen[77–79]. Each system was simulated for 500 ns in water. Each system was minimized using steepest descent with 5000 steps, followed by a relaxation of 250 ps using a 1 fs timestep, and a production run of 500 ns using a 2 fs time step. The temperature and pressure were held constant at 298 K and 1 bar using the Berendsen thermostat and barostat[80] for the relaxation step and the V-rescale thermostat[81] and Parrinello-Rahman barostat[82] for the production run. The pressure coupling was isotropic with a compressibility of 4.5×10^{-5} bar^{-1}. The temperature was coupled using τ = 1 ps during both the relaxation and production run. For pressure coupling, τ = 1 ps was set during relaxation and 5 ps during production. The electrostatics were treated with the PME algorithm[83] using a cutoff of 1.2 nm, while the van der Waals interactions were truncated, smoothly switching the force to zero between 1.0 and 1.2 nm[84]. Bonds involving hydrogen atoms were restricted using the LINCS algorithm[85].

Coarse-grained model parameterization. Martini CG models were then obtained according to the parametrization rules of Martini 3, as described elsewhere[86]. In short, atomistic simulations were mapped into CG resolution using MD Analysis[87,88] . The bonded terms were then measured and the distributions plotted. The molecule was then modelled in CG and simulated in water. Bonded distributions were fitted onto the corresponding atomistic distributions. Bead types and sizes were selected according to Martini 3 parametrization guidelines, ensuring consistency with default bead assignments for specific chemical groups[86]. These choices were validated by estimating CG octanol/water partitioning free energies, which were compared to predictors obtained via SwissADME[89] (iLOGP[90], XLOGP3[91], WLOGP[92], MLOGP[93], SILICOS-IT). The calculated partitioning free energies were obtained by thermodynamic integration as described elsewhere[86].

VBIT-4 Martini CG MD Simulations.

Unbiased CG MD. Membrane bilayers were constructed with COBY[94], which also solvated the system, neutralized it and added ions to obtain a 150 mM NaCl concentration. COBY also added the appropriate number of VBIT-4 molecules in solution. All systems were subject to the same relaxation and production protocol. First, a minimization of 5000 steps using steepest descent, followed by 10 ns of relaxation and finally at least 5 μs production run. A complex membrane composition mimicking the mitochondrial outer membrane was used (8:25:17:13:4:9:3:8:4 CHOL:POPC:DOPC:DPPC:POPE:DOPE:DPPE:POPS:POPI:DPPI) in a 15 × 15 × 17.5 nm^3 system. Prior to production, the systems underwent 5000 energy minimization steps, followed by equilibration for 10 ns using a 10 fs time step. During equilibration, VBIT-4 molecules were pulled into the membrane using flat-bottom potentials to avoid sampling the membrane adsorption process. These potentials were not applied during production run. The production runs for each system were carried out for 10 µs. Throughout the simulations, the temperatures of the lipids (including VBIT-4) and solvent (including ions) were independently maintained at 300 K using the v-rescale thermostat (τ_t = 1 ps)[81], and the pressure was kept at 1 bar using the c-rescale barostat (τ_p = 4 ps)[95] with semi-isotropic pressure coupling applied during both equilibration and production phases. Compressibility was set to 3×10^{-4} bar^{-1}. As suggested by Kim et al.[96], the cut-off distance for the short-range neighbor list was set to 1.35 nm for proper neighbor list updates.

Membrane translocation PMF. Similarly to the unbiased CG MD systems, COBY was used to build a smaller 7 × 7 × 13.5 nm^3 system, fully solvated with water and 150 mM NaCl. One VBIT-4 molecule was placed 4 nm away (determined from the center of geometry of VBIT-4) from the bilayer center along the bilayer normal and overlapping water molecules were removed. Minimization and equilibration were performed as with the unbiased simulations. At the end of the equilibration, initial configurations for the umbrella sampling windows were generated by pulling the VBIT-4 molecule through the bilayer center at a rate of 0.0001 nm/ps and a force constant of 3000 kJ/mol/nm^2. In each umbrella sampling window, a harmonic potential was applied to keep the VBIT-4 molecule in its pre-defined distance from the bilayer center with a force constant ranging from 1000 to 2000 kJ/mol/nm^2. A total of 52 windows were simulated for 2 µs and the data from the first 200 ns were discarded before applying the weighted histogram analysis method to estimate the free energy profile using GROMACS. The translocation PMF of the molecule was computed along the entire membrane normal from z = 5.25 to z = -5.25. For each replica, the PMF was symmetrized by splitting it at the membrane center and averaging both halves. The final PMF and standard deviation were obtained by averaging the symmetrized profiles across all replicas.

Polar defect formation PMF. Polar defect formation PMF was determined as described by Hub and Awasthi[52]. Small 10 × 10 × 14 nm^3 membrane bilayer systems were built using COBY, as described for the unbiased MD systems. Minimization and equilibration were performed as with the unbiased simulations. The initial frames for the umbrella sampling simulations were extracted from constant velocity pulling simulations. In these simulations, the systems were pulled from the reaction chain coordinate[52,97] $\xi_{ch} = 0.25$ to $\xi_{ch} = 1$ over 1000 ns using a force constant of 5000 kJ mol^{-1}. Nineteen umbrella windows were employed, with reference positions ranging from $\xi ch = 0.1$ to 1 in increments of 0.05, where 1 is the fully formed pore. The force constant was set to 8000 kJ mol^{-1}. Each window was simulated for 1 μs, with the initial 500 ns excluded for equilibration. Three replicas of each window were run. The potential of mean force was computed using the weighted histogram analysis method (WHAM)[98].

Cell toxicity assay

HeLa WT and VDAC1 knockout cells from Synthego were seeded at 2,500 cells/well in a 96-well plate (ThermoFisher Scientific, 165305) in DMEM (Gibco, 15607) supplemented with 10% FBS (Gibco, 10437). 200 mM VBIT-4 was prepared by adding 54.6 µL DMSO to 5 mg VBIT-4 (Selleckchem.com, S3544) and was added to the cells at a final concentration of 0-200 µM VBIT-4. After 48 hours at 37 °C and 5% CO_2, GF-AFC and bis-AAF-R110 substrates from the MultiTox-Fluor Multiplex Cytotoxicity Assay kit (Promega, G9201) were added to the cells following the manufacturer's protocol and incubated for 30 minutes at 37 °C. Viability and cytotoxicity were measured using 400/505 nm and 485/520 nm excitation/emission filters, respectively, in a CLARIOstar plate reader. Nonlinear regression curve fit was applied to calculate the IC_{50} for VBIT-4 using GraphPad Prism (version 10.1.2).

References:

(1) Gonçalves, R. P.; Buzhynskyy, N.; Prima, V.; Sturgis, J. N.; Scheuring, S. Supramolecular Assembly of VDAC in Native Mitochondrial Outer Membranes. *J. Mol. Biol.* **2007**, *369* (2), 413–418. https://doi.org/10.1016/j.jmb.2007.03.063.
(2) Hoogenboom, B. W.; Suda, K.; Engel, A.; Fotiadis, D. The Supramolecular Assemblies of Voltage-Dependent Anion Channels in the Native Membrane. *J. Mol. Biol.* **2007**, *370* (2), 246–255. https://doi.org/10.1016/j.jmb.2007.04.073.
(3) Cheng, E. H. Y.; Sheiko, T. V.; Fisher, J. K.; Craigen, W. J.; Korsmeyer, S. J. VDAC2 Inhibits BAK Activation and Mitochondrial Apoptosis. *Science* **2003**, *301* (5632), 513–517. https://doi.org/10.1126/science.1083995.
(4) Roy, S. S.; Ehrlich, A. M.; Craigen, W. J.; Hajnóczky, G. VDAC2 Is Required for Truncated BID-Induced Mitochondrial Apoptosis by Recruiting BAK to the Mitochondria. *EMBO Rep.* **2009**, *10* (12), 1341–1347. https://doi.org/10.1038/embor.2009.219.
(5) Chin, H. S.; Li, M. X.; Tan, I. K. L.; Ninnis, R. L.; Reljic, B.; Scicluna, K.; Dagley, L. F.; Sandow, J. J.; Kelly, G. L.; Samson, A. L.; Chappaz, S.; Khaw, S. L.; Chang, C.; Morokoff, A.; Brinkmann, K.; Webb, A.; Hockings, C.; Hall, C. M.; Kueh, A. J.; Ryan, M. T.; Kluck, R. M.; Bouillet, P.; Herold, M. J.; Gray, D. H. D.; Huang, D. C. S.; van Delft, M. F.; Dewson, G. VDAC2 Enables BAX to Mediate Apoptosis and Limit Tumor Development. *Nat. Commun.* **2018**, *9* (1), 4976. https://doi.org/10.1038/s41467-018-07309-4.
(6) van Delft, M. F.; Chappaz, S.; Khakham, Y.; Bui, C. T.; Debrincat, M. A.; Lowes, K. N.; Brouwer, J. M.; Grohmann, C.; Sharp, P. P.; Dagley, L. F.; Li, L.; McArthur, K.; Luo, M.-X.; Chin, H. S.; Fairlie, W. D.; Lee, E. F.; Segal, D.; Duflocq, S.; Lessene, R.; Bernard, S.; Peilleron, L.; Nguyen, T.; Miles, C.; Wan, S. S.; Lane, R. M.; Wardak, A.; Lackovic, K.; Colman, P. M.; Sandow, J. J.; Webb, A. I.; Czabotar, P. E.; Dewson, G.; Watson, K. G.; Huang, D. C. S.; Lessene, G.; Kile, B. T. A Small Molecule Interacts with VDAC2 to Block

Mouse BAK-Driven Apoptosis. *Nat. Chem. Biol.* **2019**, *15* (11), 1057–1066. https://doi.org/10.1038/s41589-019-0365-8.

(7) Sander, P.; Gudermann, T.; Schredelseker, J. A Calcium Guard in the Outer Membrane: Is VDAC a Regulated Gatekeeper of Mitochondrial Calcium Uptake? *Int. J. Mol. Sci.* **2021**, *22* (2), 946. https://doi.org/10.3390/ijms22020946.

(8) Shankar, T. S.; Ramadurai, D. K. A.; Steinhorst, K.; Sommakia, S.; Badolia, R.; Thodou Krokidi, A.; Calder, D.; Navankasattusas, S.; Sander, P.; Kwon, O. S.; Aravamudhan, A.; Ling, J.; Dendorfer, A.; Xie, C.; Kwon, O.; Cheng, E. H. Y.; Whitehead, K. J.; Gudermann, T.; Richardson, R. S.; Sachse, F. B.; Schredelseker, J.; Spitzer, K. W.; Chaudhuri, D.; Drakos, S. G. Cardiac-Specific Deletion of Voltage Dependent Anion Channel 2 Leads to Dilated Cardiomyopathy by Altering Calcium Homeostasis. *Nat. Commun.* **2021**, *12* (1), 4583. https://doi.org/10.1038/s41467-021-24869-0.

(9) Rosencrans, W. M.; Aguilella, V. M.; Rostovtseva, T. K.; Bezrukov, S. M. α-Synuclein Emerges as a Potent Regulator of VDAC-Facilitated Calcium Transport. *Cell Calcium* **2021**, *95*, 102355. https://doi.org/10.1016/j.ceca.2021.102355.

(10) Rosencrans, W. M.; Rajendran, M.; Bezrukov, S. M.; Rostovtseva, T. K. VDAC Regulation of Mitochondrial Calcium Flux: From Channel Biophysics to Disease. *Cell Calcium* **2021**, *94*, 102356. https://doi.org/10.1016/j.ceca.2021.102356.

(11) Kim, J.; Gupta, R.; Blanco, L. P.; Yang, S.; Shteinfer-Kuzmine, A.; Wang, K.; Zhu, J.; Yoon, H. E.; Wang, X.; Kerkhofs, M.; Kang, H.; Brown, A. L.; Park, S.-J.; Xu, X.; Zandee van Rilland, E.; Kim, M. K.; Cohen, J. I.; Kaplan, M. J.; Shoshan-Barmatz, V.; Chung, J. H. VDAC Oligomers Form Mitochondrial Pores to Release mtDNA Fragments and Promote Lupus-like Disease. *Science* **2019**, *366* (6472), 1531–1536. https://doi.org/10.1126/science.aav4011.

(12) Jahn, H.; Bartoš, L.; Dearden, G. I.; Dittman, J. S.; Holthuis, J. C. M.; Vácha, R.; Menon, A. K. Phospholipids Are Imported into Mitochondria by VDAC, a Dimeric Beta Barrel Scramblase. *Nat. Commun.* **2023**, *14* (1), 8115. https://doi.org/10.1038/s41467-023-43570-y.

(13) Yuan, Z.; Dewson, G.; Czabotar, P. E.; Birkinshaw, R. W. VDAC2 and the BCL-2 Family of Proteins. *Biochem. Soc. Trans.* **2021**, *49* (6), 2787–2795. https://doi.org/10.1042/BST20210753.

(14) Rovini, A. Tubulin-VDAC Interaction: Molecular Basis for Mitochondrial Dysfunction in Chemotherapy-Induced Peripheral Neuropathy. *Front. Physiol.* **2019**, *10*, 671. https://doi.org/10.3389/fphys.2019.00671.

(15) Jacobs, D.; Hoogerheide, D. P.; Rovini, A.; Jiang, Z.; Lee, J. C.; Rostovtseva, T. K.; Bezrukov, S. M. Probing Membrane Association of α-Synuclein Domains with VDAC Nanopore Reveals Unexpected Binding Pattern. *Sci. Rep.* **2019**, *9* (1), 4580. https://doi.org/10.1038/s41598-019-40979-8.

(16) Queralt-Martín, M.; Bergdoll, L.; Teijido, O.; Munshi, N.; Jacobs, D.; Kuszak, A. J.; Protchenko, O.; Reina, S.; Magrì, A.; De Pinto, V.; Bezrukov, S. M.; Abramson, J.; Rostovtseva, T. K. A Lower Affinity to Cytosolic Proteins Reveals VDAC3 Isoform-Specific Role in Mitochondrial Biology. *J. Gen. Physiol.* **2020**, *152* (2). https://doi.org/10.1085/jgp.201912501.

(17) Xu, X.; Decker, W.; Sampson, M. J.; Craigen, W. J.; Colombini, M. Mouse VDAC Isoforms Expressed in Yeast: Channel Properties and Their Roles in Mitochondrial Outer Membrane Permeability. *J. Membr. Biol.* **1999**, *170* (2), 89–102. https://doi.org/10.1007/s002329900540.

(18) Camara, A. K. S.; Zhou, Y.; Wen, P.-C.; Tajkhorshid, E.; Kwok, W.-M. Mitochondrial VDAC1: A Key Gatekeeper as Potential Therapeutic Target. *Front. Physiol.* **2017**, *8*, 460. https://doi.org/10.3389/fphys.2017.00460.

(19) Magri, A.; Messina, A. Interactions of VDAC with Proteins Involved in Neurodegenerative Aggregation: An Opportunity for Advancement on Therapeutic Molecules. *Curr. Med. Chem.* **2017**, *24* (40), 4470–4487. https://doi.org/10.2174/0929867324666170601073920.

(20) Reina, S.; De Pinto, V. Anti-Cancer Compounds Targeted to VDAC: Potential and Perspectives. *Curr. Med. Chem.* **2017**, *24* (40), 4447–4469. https://doi.org/10.2174/0929867324666170530074039.

(21) Leung, M. R.; Zenezini Chiozzi, R.; Roelofs, M. C.; Hevler, J. F.; Ravi, R. T.; Maitan, P.; Zhang, M.; Henning, H.; Bromfield, E. G.; Howes, S. C.; Gadella, B. M.; Heck, A. J. R.; Zeev-Ben-Mordehai, T. In-Cell Structures of Conserved Supramolecular Protein Arrays at the Mitochondria-Cytoskeleton Interface in Mammalian Sperm. *Proc. Natl. Acad. Sci. U. S. A.* **2021**, *118* (45), e2110996118. https://doi.org/10.1073/pnas.2110996118.

(22) Callegari, S.; Kirk, N. S.; Gan, Z. Y.; Dite, T.; Cobbold, S. A.; Leis, A.; Dagley, L. F.; Glukhova, A.; Komander, D. Structure of Human PINK1 at a Mitochondrial TOM-VDAC Array. *Science* **2025**, *388* (6744), 303–310. https://doi.org/10.1126/science.adu6445.

(23) Lafargue, E.; Duneau, J.-P.; Buzhinsky, N.; Ornelas, P.; Ortega, A.; Ravishankar, V.; Sturgis, J.; Casuso, I.; Bergdoll, L. Membrane Lipid Composition Modulates the Organization of VDAC1, a Mitochondrial Gatekeeper. *Commun. Biol.* **2025**, *8* (1), 936. https://doi.org/10.1038/s42003-025-08311-5.

(24) Ben-Hail, D.; Begas-Shvartz, R.; Shalev, M.; Shteinfer-Kuzmine, A.; Gruzman, A.; Reina, S.; De Pinto, V.; Shoshan-Barmatz, V. Novel Compounds Targeting the Mitochondrial Protein VDAC1 Inhibit Apoptosis and Protect against Mitochondrial Dysfunction. *J. Biol. Chem.* **2016**, *291* (48), 24986–25003. https://doi.org/10.1074/jbc.M116.744284.

(25) Klapper-Goldstein, H.; Verma, A.; Elyagon, S.; Gillis, R.; Murninkas, M.; Pittala, S.; Paul, A.; Shoshan-Barmatz, V.; Etzion, Y. VDAC1 in the Diseased Myocardium and the Effect of VDAC1-Interacting Compound on Atrial Fibrosis Induced by Hyperaldosteronism. *Sci. Rep.* **2020**, *10* (1), 22101. https://doi.org/10.1038/s41598-020-79056-w.

(26) Shteinfer-Kuzmine, A.; Argueti-Ostrovsky, S.; Leyton-Jaimes, M. F.; Anand, U.; Abu-Hamad, S.; Zalk, R.; Shoshan-Barmatz, V.; Israelson, A. Targeting the Mitochondrial Protein VDAC1 as a Potential Therapeutic Strategy in ALS. *Int. J. Mol. Sci.* **2022**, *23* (17), 9946. https://doi.org/10.3390/ijms23179946.

(27) Verma, A.; Pittala, S.; Alhozeel, B.; Shteinfer-Kuzmine, A.; Ohana, E.; Gupta, R.; Chung, J. H.; Shoshan-Barmatz, V. The Role of the Mitochondrial Protein VDAC1 in Inflammatory Bowel Disease: A Potential Therapeutic Target. *Mol. Ther. J. Am. Soc. Gene Ther.* **2022**, *30* (2), 726–744. https://doi.org/10.1016/j.ymthe.2021.06.024.

(28) Verma, A.; Shteinfer-Kuzmine, A.; Kamenetsky, N.; Pittala, S.; Paul, A.; Nahon Crystal, E.; Ouro, A.; Chalifa-Caspi, V.; Pandey, S. K.; Monsonego, A.; Vardi, N.; Knafo, S.; Shoshan-Barmatz, V. Targeting the Overexpressed Mitochondrial Protein VDAC1 in a Mouse Model of Alzheimer's Disease Protects against Mitochondrial Dysfunction and Mitigates Brain Pathology. *Transl. Neurodegener.* **2022**, *11* (1), 58. https://doi.org/10.1186/s40035-022-00329-7.

(29) Belosludtsev, K. N.; Serov, D. A.; Ilzorkina, A. I.; Starinets, V. S.; Dubinin, M. V.; Talanov, E. Y.; Karagyaur, M. N.; Primak, A. L.; Belosludtseva, N. V. Pharmacological and Genetic Suppression of VDAC1 Alleviates the Development of Mitochondrial Dysfunction in Endothelial and Fibroblast Cell Cultures upon Hyperglycemic Conditions. *Antioxid. Basel Switz.* **2023**, *12* (7), 1459. https://doi.org/10.3390/antiox12071459.

(30) Mohammad Al-Amily, I.; Sjögren, M.; Duner, P.; Tariq, M.; Wollheim, C. B.; Salehi, A. Ablation of GPR56 Causes β-Cell Dysfunction by ATP Loss through Mistargeting of Mitochondrial VDAC1 to the Plasma Membrane. *Biomolecules* **2023**, *13* (3), 557. https://doi.org/10.3390/biom13030557.

(31) Tariq, M.; Sjögren, M.; Salehi, A. Sulindac Prevents Increased Mitochondrial VDAC1 Expression and Cell Surface Mistargeting Induced by Pathological Conditions in Retinal Cells. *Biochem. Biophys. Res. Commun.* **2024**, *739*, 150558. https://doi.org/10.1016/j.bbrc.2024.150558.

(32) Wei, S.-N.; Zhang, H.; Lu, Y.; Yu, H.-J.; Ma, T.; Wang, S.-N.; Yang, K.; Tian, M.-L.; Huang, A.-H.; Wang, W.; Li, F.-S.; Li, Y.-W. Microglial Voltage-Dependent Anion Channel 1 Signaling Modulates Sleep Deprivation-Induced Transition to Chronic Postsurgical Pain. *Sleep* **2023**, *46* (11), zsad039. https://doi.org/10.1093/sleep/zsad039.

(33) Luo, X.; Yue, J. VDAC1 Inhibition Mitigates Inflammatory Status and Oxidative Stress in Epileptic Mice Treated with the Ketogenic Diet. *Neurochem. Res.* **2025**, *50* (2), 118. https://doi.org/10.1007/s11064-025-04366-2.

(34) Gorny, H.; Mularoni, A.; Delcros, J.-G.; Freton, C.; Preto, J.; Krimm, I. Combining Nano-Differential Scanning Fluorimetry and Microscale Thermophoresis to Investigate VDAC1 Interaction with Small Molecules. *J. Enzyme Inhib. Med. Chem.* **2023**, *38* (1), 2121821. https://doi.org/10.1080/14756366.2022.2121821.

(35) de Kroon, A. I.; Dolis, D.; Mayer, A.; Lill, R.; de Kruijff, B. Phospholipid Composition of Highly Purified Mitochondrial Outer Membranes of Rat Liver and Neurospora Crassa. Is Cardiolipin Present in the Mitochondrial Outer Membrane? *Biochim. Biophys. Acta* **1997**, *1325* (1), 108–116. https://doi.org/10.1016/s0005-2736(96)00240-4.

(36) Terrones, O.; Antonsson, B.; Yamaguchi, H.; Wang, H.-G.; Liu, J.; Lee, R. M.; Herrmann, A.; Basañez, G. Lipidic Pore Formation by the Concerted Action of Proapoptotic BAX and tBID. *J. Biol. Chem.* **2004**, *279* (29), 30081–30091. https://doi.org/10.1074/jbc.M313420200.

(37) Colombini, M. Ceramide Channels. In *Bioactive Ceramides in Health and Disease*; Stiban, J., Ed.; Advances in Experimental Medicine and Biology; Springer International Publishing: Cham, 2019; Vol. 1159, pp 33–48. https://doi.org/10.1007/978-3-030-21162-2_3.

(38) Anosov, A. A.; Smirnova, E. Yu.; Ryleeva, E. D.; Gligonov, I. A.; Korepanova, E. A.; Sharakshane, A. A. Estimation of the Parameters of the Smoluchowski Equation Describing the Occurrence of Pores in a Bilayer Lipid Membrane under Soft Poration. *Eur. Phys. J. E* **2020**, *43* (10), 66. https://doi.org/10.1140/epje/i2020-11989-0.

(39) Steringer, J. P.; Bleicken, S.; Andreas, H.; Zacherl, S.; Laussmann, M.; Temmerman, K.; Contreras, F. X.; Bharat, T. A. M.; Lechner, J.; Müller, H.-M.; Briggs, J. A. G.; García-Sáez, A. J.; Nickel, W. Phosphatidylinositol 4,5-Bisphosphate (PI(4,5)P2)-Dependent Oligomerization of Fibroblast Growth Factor 2 (FGF2) Triggers the Formation of a Lipidic Membrane Pore Implicated in Unconventional Secretion. *J. Biol. Chem.* **2012**, *287* (33), 27659–27669. https://doi.org/10.1074/jbc.M112.381939.

(40) Ashrafuzzaman, M.; Tseng, C.; Duszyk, M.; Tuszynski, J. A. Chemotherapy Drugs Form Ion Pores in Membranes Due to Physical Interactions with Lipids. *Chem. Biol. Drug Des.* **2012**, *80* (6), 992–1002. https://doi.org/10.1111/cbdd.12060.

(41) Perini, D. A.; Aguilella-Arzo, M.; Alcaraz, A.; Perálvarez-Marín, A.; Queralt-Martín, M. Dynorphin A Induces Membrane Permeabilization by Formation of Proteolipidic Pores. Insights from Electrophysiology and Computational Simulations. *Comput. Struct. Biotechnol. J.* **2022**, *20*, 230–240. https://doi.org/10.1016/j.csbj.2021.12.021.

(42) Serra-Batiste, M.; Ninot-Pedrosa, M.; Bayoumi, M.; Gairí, M.; Maglia, G.; Carulla, N. Aβ42 Assembles into Specific β-Barrel Pore-Forming Oligomers in Membrane-Mimicking Environments. *Proc. Natl. Acad. Sci.* **2016**, *113* (39), 10866–10871. https://doi.org/10.1073/pnas.1605104113.

(43) Roucou, X.; Rostovtseva, T.; Montessuit, S.; Martinou, J.-C.; Antonsson, B. Bid Induces Cytochrome C-Impermeable Bax Channels in Liposomes. *Biochem. J.* **2002**, *363* (3), 547–552. https://doi.org/10.1042/bj3630547.

(44) Gurnev, P. A.; Queralt-Martin, M.; Aguilella, V. M.; Rostovtseva, T. K.; Bezrukov, S. M. Probing Tubulin-Blocked State of VDAC by Varying Membrane Surface Charge. *Biophys. J.* **2012**, *102* (9), 2070–2076. https://doi.org/10.1016/j.bpj.2012.03.058.

(45) Souza, P. C. T.; Alessandri, R.; Barnoud, J.; Thallmair, S.; Faustino, I.; Grünewald, F.; Patmanidis, I.; Abdizadeh, H.; Bruininks, B. M. H.; Wassenaar, T. A.; Kroon, P. C.; Melcr, J.; Nieto, V.; Corradi, V.; Khan, H. M.; Domański, J.; Javanainen, M.; Martinez-Seara, H.; Reuter, N.; Best, R. B.; Vattulainen, I.; Monticelli, L.; Periole, X.; Tieleman, D. P.; de Vries, A. H.; Marrink, S. J. Martini 3: A General Purpose Force Field for Coarse-Grained Molecular Dynamics. *Nat. Methods* **2021**, *18* (4), 382–388. https://doi.org/10.1038/s41592-021-01098-3.

(46) Bieker, S.; Timme, M.; Woge, N.; Hassan, D. G.; Brown, C. M.; Marrink, S. J.; Melo, M. N.; Holthuis, J. C. M. Hexokinase-I Directly Binds to a Charged Membrane-Buried Glutamate of Mitochondrial VDAC1 and VDAC2. bioRxiv July 23, 2024, p 2024.07.22.604557. https://doi.org/10.1101/2024.07.22.604557.

(47) Dadsena, S.; Bockelmann, S.; Mina, J. G. M.; Hassan, D. G.; Korneev, S.; Razzera, G.; Jahn, H.; Niekamp, P.; Müller, D.; Schneider, M.; Tafesse, F. G.; Marrink, S. J.; Melo, M. N.; Holthuis, J. C. M. Ceramides Bind VDAC2 to Trigger Mitochondrial Apoptosis. *Nat. Commun.* **2019**, *10* (1), 1832. https://doi.org/10.1038/s41467-019-09654-4.

(48) Mazzobre, M. F.; Román, M. V.; Mourelle, A. F.; Corti, H. R. Octanol-Water Partition Coefficient of Glucose, Sucrose, and Trehalose. *Carbohydr. Res.* **2005**, *340* (6), 1207–1211. https://doi.org/10.1016/j.carres.2004.12.038.

(49) Fornasier, F.; Souza, L. M. P.; Souza, F. R.; Reynaud, F.; Pimentel, A. S. Lipophilicity of Coarse-Grained Cholesterol Models. *J. Chem. Inf. Model.* **2020**, *60* (2), 569–577. https://doi.org/10.1021/acs.jcim.9b00830.

(50) Avdeef, A. pH-Metric Log P. II: Refinement of Partition Coefficients and Ionization Constants of Multiprotic Substances. *J. Pharm. Sci.* **1993**, *82* (2), 183–190. https://doi.org/10.1002/jps.2600820214.

(51) Pedersen, K. B.; Ingólfsson, H. I.; Ramirez-Echemendia, D. P.; Borges-Araújo, L.; Andreasen, M. D.; Empereur-Mot, C.; Melcr, J.; Ozturk, T. N.; Bennett, D. W.; Kjølbye, L. R.; others. The Martini 3 Lipidome: Expanded and Refined Parameters Improve Lipid Phase Behavior. **2024**.

(52) Hub, J. S.; Awasthi, N. Probing a Continuous Polar Defect: A Reaction Coordinate for Pore Formation in Lipid Membranes. *J. Chem. Theory Comput.* **2017**, *13* (5), 2352–2366. https://doi.org/10.1021/acs.jctc.7b00106.

(53) Luo, X.; Yue, J. VDAC1 Inhibition Mitigates Inflammatory Status and Oxidative Stress in Epileptic Mice Treated with the Ketogenic Diet. *Neurochem. Res.* **2025**, *50* (2), 118. https://doi.org/10.1007/s11064-025-04366-2.

(54) Liu, H.; Fan, H.; He, P.; Zhuang, H.; Liu, X.; Chen, M.; Zhong, W.; Zhang, Y.; Zhen, C.; Li, Y.; Jiang, H.; Meng, T.; Xu, Y.; Zhao, G.; Feng, D. Prohibitin 1 Regulates MTDNA Release and Downstream Inflammatory Responses. *EMBO J.* **2022**, *41* (24), e111173. https://doi.org/10.15252/embj.2022111173.

(55) Dadsena, S.; Jenner, A.; García-Sáez, A. J. Mitochondrial Outer Membrane Permeabilization at the Single Molecule Level. *Cell. Mol. Life Sci. CMLS* **2021**. https://doi.org/10.1007/s00018-021-03771-4.

(56) Keinan, N.; Tyomkin, D.; Shoshan-Barmatz, V. Oligomerization of the Mitochondrial Protein Voltage-Dependent Anion Channel Is Coupled to the Induction of Apoptosis. *Mol. Cell. Biol.* **2010**, *30* (24), 5698–5709. https://doi.org/10.1128/MCB.00165-10.

(57) Rostovtseva, T. K.; Sheldon, K. L.; Hassanzadeh, E.; Monge, C.; Saks, V.; Bezrukov, S. M.; Sackett, D. L. Tubulin Binding Blocks Mitochondrial Voltage-Dependent Anion Channel and Regulates Respiration. *Proc. Natl. Acad. Sci. U. S. A.* **2008**, *105* (48), 18746–18751. https://doi.org/10.1073/pnas.0806303105.

(58) Rostovtseva, T. K.; Gurnev, P. A.; Protchenko, O.; Hoogerheide, D. P.; Yap, T. L.; Philpott, C. C.; Lee, J. C.; Bezrukov, S. M. α-Synuclein Shows High Affinity Interaction with Voltage-Dependent Anion Channel, Suggesting Mechanisms of Mitochondrial Regulation and Toxicity in Parkinson Disease. *J. Biol. Chem.* **2015**, *290* (30), 18467–18477. https://doi.org/10.1074/jbc.M115.641746.

(59) Bergdoll, L. A.; Lerch, M. T.; Patrick, J. W.; Belardo, K.; Altenbach, C.; Bisignano, P.; Laganowsky, A.; Grabe, M.; Hubbell, W. L.; Abramson, J. Protonation State of Glutamate 73 Regulates the Formation of a Specific Dimeric Association of mVDAC1. *Proc. Natl. Acad. Sci. U. S. A.* **2018**, *115* (2), E172–E179. https://doi.org/10.1073/pnas.1715464115.

(60) Jang, S.-K.; Ahn, S. H.; Kim, G.; Kim, S.; Hong, J.; Park, K. S.; Park, I.-C.; Jin, H.-O. Inhibition of VDAC1 Oligomerization Blocks Cysteine Deprivation-Induced Ferroptosis via Mitochondrial ROS Suppression. *Cell Death Dis.* **2024**, *15* (11), 811. https://doi.org/10.1038/s41419-024-07216-1.

(61) Oflaz, F. E.; Bondarenko, A. I.; Trenker, M.; Waldeck-Weiermair, M.; Gottschalk, B.; Bernhart, E.; Koshenov, Z.; Radulović, S.; Rost, R.; Hirtl, M.; Pilic, J.; Karunanithi Nivedita, A.; Sagintayev, A.; Leitinger, G.; Brachvogel, B.; Summerauer, S.; Shoshan-Barmatz, V.; Malli, R.; Graier, W. F. Annexin A5 Controls VDAC1-Dependent Mitochondrial Ca2+ Homeostasis and Determines Cellular Susceptibility to Apoptosis. *EMBO J.* **2025**, *44* (12), 3413–3447. https://doi.org/10.1038/s44318-025-00454-9.

(62) Pereira-Leite, C.; Lopes-de-Campos, D.; Fontaine, P.; Cuccovia, I. M.; Nunes, C.; Reis, S. Licofelone-DPPC Interactions: Putting Membrane Lipids on the Radar of Drug Development. *Molecules* **2019**, *24* (3), 516. https://doi.org/10.3390/molecules24030516.

(63) Lopes-de-Campos, D.; Pereira-Leite, C.; Fontaine, P.; Coutinho, A.; Prieto, M.; Sarmento, B.; Jakobtorweihen, S.; Nunes, C.; Reis, S. Interface-Mediated Mechanism of Action-The Root of the Cytoprotective Effect of Immediate-Release Omeprazole. *J. Med. Chem.* **2021**, *64* (8), 5171–5184. https://doi.org/10.1021/acs.jmedchem.1c00251.

(64) Belosludtsev, K. N.; Ilzorkina, A. I.; Matveeva, L. A.; Chulkov, A. V.; Semenova, A. A.; Dubinin, M. V.; Belosludtseva, N. V. Effect of VBIT-4 on the Functional Activity of Isolated Mitochondria and Cell Viability. *Biochim. Biophys. Acta Biomembr.* **2024**, *1866* (5), 184329. https://doi.org/10.1016/j.bbamem.2024.184329.

(65) Finichiu, P. G.; James, A. M.; Larsen, L.; Smith, R. A. J.; Murphy, M. P. Mitochondrial Accumulation of a Lipophilic Cation Conjugated to an Ionisable Group Depends on Membrane Potential, pH Gradient and pK a: Implications for the Design of Mitochondrial Probes and Therapies. *J. Bioenerg. Biomembr.* **2013**, *45* (1–2), 165–173. https://doi.org/10.1007/s10863-012-9493-5.

(66) Dearden, G. I.; Ravishankar, V.; Sakata, K.-T.; Menon, A. K.; Bergdoll, L. Protocol for the Production and Reconstitution of VDAC1 for Functional Assays. *STAR Protoc.* **2024**, *5* (3), 103240. https://doi.org/10.1016/j.xpro.2024.103240.

(67) Ando, T.; Kodera, N.; Takai, E.; Maruyama, D.; Saito, K.; Toda, A. A High-Speed Atomic Force Microscope for Studying Biological Macromolecules. *Proc. Natl. Acad. Sci. U. S. A.* **2001**, *98* (22), 12468–12472. https://doi.org/10.1073/pnas.211400898.

(68) Schneider, C. A.; Rasband, W. S.; Eliceiri, K. W. NIH Image to ImageJ: 25 Years of Image Analysis. *Nat. Methods* **2012**, *9* (7), 671–675. https://doi.org/10.1038/nmeth.2089.

(69) Horcas, I.; Fernández, R.; Gómez-Rodríguez, J. M.; Colchero, J.; Gómez-Herrero, J.; Baro, A. M. WSXM: A Software for Scanning Probe Microscopy and a Tool for Nanotechnology. *Rev. Sci. Instrum.* **2007**, *78* (1), 013705. https://doi.org/10.1063/1.2432410.

(70) Ritchie, T. K.; Grinkova, Y. V.; Bayburt, T. H.; Denisov, I. G.; Zolnerciks, J. K.; Atkins, W. M.; Sligar, S. G. Chapter 11 - Reconstitution of Membrane Proteins in Phospholipid Bilayer Nanodiscs. *Methods Enzymol.* **2009**, *464*, 211–231. https://doi.org/10.1016/S0076-6879(09)64011-8.

(71) Rostovtseva, T. K.; Kazemi, N.; Weinrich, M.; Bezrukov, S. M. Voltage Gating of VDAC Is Regulated by Nonlamellar Lipids of Mitochondrial Membranes. *J. Biol. Chem.* **2006**, *281* (49), 37496–37506. https://doi.org/10.1074/jbc.M602548200.
(72) Narahari, A. K.; Kreutzberger, A. J.; Gaete, P. S.; Chiu, Y.-H.; Leonhardt, S. A.; Medina, C. B.; Jin, X.; Oleniacz, P. W.; Kiessling, V.; Barrett, P. Q.; Ravichandran, K. S.; Yeager, M.; Contreras, J. E.; Tamm, L. K.; Bayliss, D. A. ATP and Large Signaling Metabolites Flux through Caspase-Activated Pannexin 1 Channels. *eLife* **2021**, *10*, e64787. https://doi.org/10.7554/eLife.64787.
(73) Ujwal, R.; Cascio, D.; Colletier, J.-P.; Faham, S.; Zhang, J.; Toro, L.; Ping, P.; Abramson, J. The Crystal Structure of Mouse VDAC1 at 2.3 A Resolution Reveals Mechanistic Insights into Metabolite Gating. *Proc. Natl. Acad. Sci. U. S. A.* **2008**, *105* (46), 17742–17747. https://doi.org/10.1073/pnas.0809634105.
(74) Queralt-Martín, M.; Bergdoll, L.; Jacobs, D.; Bezrukov, S. M.; Abramson, J.; Rostovtseva, T. K. Assessing the Role of Residue E73 and Lipid Headgroup Charge in VDAC1 Voltage Gating. *Biochim. Biophys. Acta Bioenerg.* **2019**, *1860* (1), 22–29. https://doi.org/10.1016/j.bbabio.2018.11.001.
(75) Teijido, O.; Rappaport, S. M.; Chamberlin, A.; Noskov, S. Y.; Aguilella, V. M.; Rostovtseva, T. K.; Bezrukov, S. M. Acidification Asymmetrically Affects Voltage-Dependent Anion Channel Implicating the Involvement of Salt Bridges. *J. Biol. Chem.* **2014**, *289* (34), 23670–23682. https://doi.org/10.1074/jbc.M114.576314.
(76) Rappaport, S. M.; Teijido, O.; Hoogerheide, D. P.; Rostovtseva, T. K.; Berezhkovskii, A. M.; Bezrukov, S. M. Conductance Hysteresis in the Voltage-Dependent Anion Channel. *Eur. Biophys. J. EBJ* **2015**, *44* (6), 465–472. https://doi.org/10.1007/s00249-015-1049-2.
(77) Dodda, L. S.; Cabeza de Vaca, I.; Tirado-Rives, J.; Jorgensen, W. L. LigParGen Web Server: An Automatic OPLS-AA Parameter Generator for Organic Ligands. *Nucleic Acids Res.* **2017**, *45* (W1), W331–W336. https://doi.org/10.1093/nar/gkx312.
(78) Dodda, L. S.; Vilseck, J. Z.; Tirado-Rives, J.; Jorgensen, W. L. 1.14*CM1A-LBCC: Localized Bond-Charge Corrected CM1A Charges for Condensed-Phase Simulations. *J. Phys. Chem. B* **2017**, *121* (15), 3864–3870. https://doi.org/10.1021/acs.jpcb.7b00272.
(79) Jorgensen, W. L.; Tirado-Rives, J. Potential Energy Functions for Atomic-Level Simulations of Water and Organic and Biomolecular Systems. *Proc. Natl. Acad. Sci. U. S. A.* **2005**, *102* (19), 6665–6670. https://doi.org/10.1073/pnas.0408037102.
(80) Berendsen, H. J. C.; Postma, J. P. M.; van Gunsteren, W. F.; Di Nola, A.; Haak, J. R. Molecular Dynamics with Coupling to an External Bath. *J. Chem. Phys.* **1984**, *81* (8), 3684–3690. https://doi.org/10.1063/1.448118.
(81) Bussi, G.; Donadio, D.; Parrinello, M. Canonical Sampling through Velocity Rescaling. *J. Chem. Phys.* **2007**, *126* (1), 014101. https://doi.org/10.1063/1.2408420.
(82) Parrinello, M.; Rahman, A. Polymorphic Transitions in Single Crystals: A New Molecular Dynamics Method. *Journal of applied physics*. 52nd ed. 1981, pp 7182–7190.
(83) Darden, T.; York, D.; Pedersen, L. Particle Mesh Ewald: An N·log(N) Method for Ewald Sums in Large Systems. *Journal of Chemical Physics*. 98th ed. 1993, pp 10089–10092.
(84) Páll, S.; Hess, B. A Flexible Algorithm for Calculating Pair Interactions on SIMD Architectures. *Comput. Phys. Commun.* **2013**, *184* (12), 2641–2650. https://doi.org/10.1016/j.cpc.2013.06.003.
(85) Hess, B.; Bekker, H.; Berendsen, H. J. C.; Fraaije, J. G. E. M. LINCS: A Linear Constraint Solver for Molecular Simulations. *J. Comput. Chem.* **1997**, *18* (12), 1463–1472. https://doi.org/10.1002/(SICI)1096-987X(199709)18:12<1463::AID-JCC4>3.0.CO;2-H.
(86) Souza, P. C. T.; Thallmair, S.; Conflitti, P.; Ramírez-Palacios, C.; Alessandri, R.; Raniolo, S.; Limongelli, V.; Marrink, S. J. Protein-Ligand Binding with the Coarse-Grained Martini Model. *Nat. Commun.* **2020**, *11* (1), 3714. https://doi.org/10.1038/s41467-020-17437-

5.
(87) Gowers, R. J.; Linke, M.; Barnoud, J.; Reddy, T. J. E.; Melo, M. N.; Seyler, S. L.; Domanski, J.; Dotson, D. L.; Buchoux, S.; Kenney, I. M.; Beckstein, O. MDAnalysis: A Python Package for the Rapid Analysis of Molecular Dynamics Simulations. In *Report Number: LA-UR-19-29136*; Research Org.: Los Alamos National Laboratory (LANL), Los Alamos, NM (United States), 2019. https://doi.org/10.25080/Majora-629e541a-00e.
(88) Michaud-Agrawal, N.; Denning, E. J.; Woolf, T. B.; Beckstein, O. MDAnalysis: A Toolkit for the Analysis of Molecular Dynamics Simulations. *J. Comput. Chem.* **2011**, *32* (10), 2319–2327. https://doi.org/10.1002/jcc.21787.
(89) Daina, A.; Michielin, O.; Zoete, V. SwissADME: A Free Web Tool to Evaluate Pharmacokinetics, Drug-Likeness and Medicinal Chemistry Friendliness of Small Molecules. *Sci. Rep.* **2017**, *7*, 42717. https://doi.org/10.1038/srep42717.
(90) Daina, A.; Michielin, O.; Zoete, V. iLOGP: A Simple, Robust, and Efficient Description of n-Octanol/Water Partition Coefficient for Drug Design Using the GB/SA Approach. *J. Chem. Inf. Model.* **2014**, *54* (12), 3284–3301. https://doi.org/10.1021/ci500467k.
(91) Cheng, T.; Zhao, Y.; Li, X.; Lin, F.; Xu, Y.; Zhang, X.; Li, Y.; Wang, R.; Lai, L. Computation of Octanol-Water Partition Coefficients by Guiding an Additive Model with Knowledge. *J. Chem. Inf. Model.* **2007**, *47* (6), 2140–2148. https://doi.org/10.1021/ci700257y.
(92) Wildman, S. A.; Crippen, G. M. Prediction of Physicochemical Parameters by Atomic Contributions. *J. Chem. Inf. Comput. Sci.* **1999**, *39* (5), 868–873. https://doi.org/10.1021/ci990307l.
(93) Lipinski, C. A.; Lombardo, F.; Dominy, B. W.; Feeney, P. J. Experimental and Computational Approaches to Estimate Solubility and Permeability in Drug Discovery and Development Settings. *Adv. Drug Deliv. Rev.* **2001**, *46* (1–3), 3–26. https://doi.org/10.1016/s0169-409x(00)00129-0.
(94) Andreasen, M. D.; Souza, P. C. T.; Schiøtt, B.; Zuzic, L. Creating Coarse-Grained Systems with COBY: Towards Higher Accuracy in Membrane Complexity. *bioRxiv* **2024**. https://doi.org/10.1101/2024.07.23.604601.
(95) Bernetti, M.; Bussi, G. Pressure Control Using Stochastic Cell Rescaling. *J. Chem. Phys.* **2020**, *153* (11), 114107. https://doi.org/10.1063/5.0020514.
(96) Kim, H.; Fábián, B.; Hummer, G. Neighbor List Artifacts in Molecular Dynamics Simulations. *J. Chem. Theory Comput.* **2023**, *19* (23), 8919–8929. https://doi.org/10.1021/acs.jctc.3c00777.
(97) Awasthi, N.; Hub, J. S. Free-Energy Calculations of Pore Formation in Lipid Membranes. In *Biomembrane Simulations*; CRC Press, 2019; pp 109–124.
(98) Kumar, S.; Rosenberg, J. M.; Bouzida, D.; Swendsen, R. H.; Kollman, P. A. THE Weighted Histogram Analysis Method for Free-Energy Calculations on Biomolecules. I. The Method. *J. Comput. Chem.* **1992**, *13* (8), 1011–1021.

References: